Distinguishing Classical and Quantum Models for the D-Wave Device

Walter Vinci,[1,2,*] Tameem Albash,[3,4,*] Anurag Mishra,[3,4] Paul A. Warburton,[1,5] and Daniel A. Lidar[3,4,6,7]

[1]*London Centre for Nanotechnology, University College London, WC1H 0AH London, UK*
[2]*Computer Science, University College London, WC1E 6BT London, UK*
[3]*Department of Physics and Astronomy, University of Southern California, Los Angeles, California 90089, USA*
[4]*Center for Quantum Information Science & Technology, University of Southern California, Los Angeles, California 90089, USA*
[5]*Department of Electronic & Electrical Engineering, University College London, WC1E 7JE London, UK*
[6]*Department of Electrical Engineering, University of Southern California, Los Angeles, California 90089, USA*
[7]*Department of Chemistry, University of Southern California, Los Angeles, California 90089, USA*

Recently the question of whether the D-Wave processors exhibit large-scale quantum behavior or can be described by a classical model has attracted significant interest. In this work we address this question by studying a 503 qubit D-Wave Two device as a "black box", i.e., by studying its input-output behavior. We examine three candidate classical models and one quantum model, and compare their predictions to experiments we have performed on the device using groups of up to 40 qubits. The candidate classical models are simulated annealing, spin dynamics, a recently proposed hybrid O(2) rotor-Monte Carlo model, and three modified versions thereof. The quantum model is an adiabatic Markovian master equation derived in the weak coupling limit of an open quantum system. Our experiments realize an evolution from a transverse field to an Ising Hamiltonian, with a final-time degenerate ground state that splits into two types of states we call "isolated" and "clustered." We study the population ratio of the isolated and clustered states as a function of the overall energy scale of the Ising term, and the distance between the final state and the Gibbs state, and find that these are sensitive probes that distinguish the classical models from one another and from both the experimental data and the master equation. The classical models are all found to disagree with the data, while the master equation agrees with the experiment without fine-tuning, and predicts mixed state entanglement at intermediate evolution times. This suggests that an open system quantum dynamical description of the D-Wave device is well-justified even in the presence of relevant thermal excitations and fast single-qubit decoherence.

I. INTRODUCTION

How can one determine whether a given "black box" is quantum or classical [1]? A case in point are the devices built by D-Wave [2–4]. These devices are commercial computers which the user can only access via an input-output interface. Reports [5–7] that the D-Wave devices implement quantum annealing (QA) with hundreds of qubits have attracted much attention recently, and have also generated considerable debate [8–10]. At stake is the question of whether the experimental evidence suffices to rule out classical models, and whether a quantum model can be found that is in full agreement with the evidence. The D-Wave devices operate at a nonzero temperature that can be comparable to the energy gap from the ground state, so one might expect that thermal excitations act to drive the system out of its ground state, potentially causing the annealing process to be dominated by thermal fluctuations rather than by quantum tunneling. Furthermore, the coupling to the environment should cause decoherence, potentially resulting in the loss of any quantum speedup. This issue was recently studied in Refs. [6, 7], where data from a 108-qubit D-Wave One (DW1) device was compared to numerical simulations implementing classical simulated annealing (SA), simulated quantum annealing (SQA) using quantum Monte Carlo, and a quantum adiabatic master equation (ME) derived in Ref. [11]. These studies demonstrated that SA correlates poorly with the experimental data, while the ME (in Ref. [6]) and SQA (in Ref. [7]) are in good agreement with the same data. Specifically, the 8-qubit "quantum signature" Hamiltonian introduced in Ref. [6] has a 17-fold degenerate ground state that splits into a single "isolated" state and a 16-fold degenerate "cluster," with the population in the former suppressed relative to the latter according to the ME but enhanced according to SA; the experiment agreed with the ME prediction [6]. Subsequently, Ref. [7] rejected SA on much larger problem sizes by showing that the success probability distribution it predicts for random Ising instances on up to 108 spin variables is unimodal, while the experimental data and SQA both give rise to a bimodal distribution. This was interpreted as positive evidence for the hypothesis that the device implements quantum annealing.

However, interesting objections to the latter interpretation were raised in Refs. [9, 12], where it was argued that there are other classical models that also agree with the experimental data of Refs. [6, 7]. First, Smolin and Smith [9] pointed out that a classical spin-dynamics model of O(2) rotors or O(3) vectors could be tuned to mimic the suppression of the isolated ground state found in Ref. [6] and the bimodal success probability histograms for random Ising instances found in Ref. [7]. Shortly thereafter this classical model was rejected in Ref. [10] by demonstrating that the classical SD model correlates poorly with the success probabilities measured for random Ising instances, while SQA correlates very well. In response, a new hybrid model where the spin dynamics are governed by Monte Carlo updates was very recently proposed by Shin, Smolin, Smith, and Vazirani (SSSV) [12], that correlates as well with the DW1 success probabilities for random Ising instances as SQA. In this model the qubits are replaced

* These two authors contributed equally.

by O(2) rotors with classical Monte Carlo updates along the annealing schedule of the D-Wave device. This can be interpreted as a model of "qubits" (via the standard SU(2) to SO(3) mapping) without any entanglement, updated at each time step to the classical thermal equilibrium state determined by the instantaneous Hamiltonian. Moreover, the hybrid model correlates almost perfectly with SQA, suggesting that the SSSV model is a classical analogue of a mean-field approximation to SQA, and that this approximation is very accurate for the set of problems solved by the DW1 in Ref. [7].[1]

At this point it is important to note that recent work already established that 8-qubit entangled ground states are formed during the course of the annealing evolution [13]. This demonstration of entanglement was done outside of the "black-box" paradigm we are considering here (the experiment had access to the internal workings of the D-Wave device), and is, of course, a crucial demonstration of nonclassicality. However, it does not necessarily imply that nonclassical effects play a role in deciding the *final outcome* of a computation performed by the D-Wave devices. It is the latter that we are concerned with in this work, and it is the fundamental reason we are interested in the "black-box" paradigm.

Here we show that none of the three classical models introduced to date matches new data we obtained from the D-Wave Two (DW2) device using a generalized "quantum signature" Hamiltonian on up to 40 qubits, featuring a "noise control knob". At the same time the ME matches the new data well. Thus our results confirm the earlier rejection of the SA and SD models—this is of independent interest since the "quantum signature" provided in Ref. [6] for the DW1 had remained in question in light of the SD-based critique of Ref. [9])—and also serve to reject the new SSSV model [12] for system sizes of at up to 40 qubits, by demonstrating that it does not match the experimental results at high "noise" values. To check the robustness of this conclusion we also consider three modified versions of the SSSV model, which can be understood as either "decohering" or forcing the O(2) rotors into classical Ising spins, and find that these modified SSSV models do not match the experimental data either. This leaves open the possibility that a classical model can be found which will match the experimental data after fine-tuning. In contrast, the ME requires no fine-tuning. Since our quantum signature based test does not provide a no-go result for classical models (unlike, e.g., Bell's inequality [14]), this kind of distinction between agreement via a "natural" quantum model and via a fine-tuned classical model is, perhaps, the best that can be hoped for in our approach in terms of distinguishing quantum and classical models.

The "quantum signature" Hamiltonian we consider here interpolates between a transverse field and a classical Ising Hamiltonian with a controllable overall energy scale, acting as an effective (inverse temperature) "noise control knob." The Ising Hamiltonian is defined in Sec. II and is a direct generalization of the Hamiltonian introduced in Ref. [6]. Decreasing its energy scale amounts to increasing thermal excitations, enabling us to drive the D-Wave processor between qualitatively distinct regimes. At the largest energy scale available, the annealing process appears to be dominated by coherent quantum effects, and thermal fluctuations are negligible. As the energy scale is decreased, thermal excitations become more relevant, and for a sufficiently small energy scale, the system behaves more like a classical annealer based on incoherent Ising spins. Nevertheless, at all energy scales the system is very well described by the ME. This suggests that an open system quantum dynamical description of the D-Wave device is well-justified even in the presence of relevant thermal excitations and fast single-qubit decoherence, at least for the Hamiltonians studied here.

The structure of this paper is as follows. We provide theoretical background on the quantum signature Hamiltonian—our workhorse in this study—in Sec. II. We analyze the effect of tuning the thermal noise via three different mechanisms (magnitude of the final Hamiltonian, annealing time, and system size) in Sec. III. Our main results are presented in Sec. IV, where we establish the input-output characteristics of the D-Wave device that allow us to assess the classical models, and confirm the agreement with an open quantum system description via the adiabatic quantum master equation. We demonstrate that the latter predicts that an entangled ground state is formed during the course of the annealing evolution. We discuss the results in Sec. V and conclude in Sec. VI. An appendix provides further technical details.

II. THEORETICAL BACKGROUND

Quantum and classical annealing are powerful techniques for solving hard optimization problems, whether as simulation methods or as physical devices. The general *simulation* strategy is to implement an "escape" rule from local minima of an energy or penalty function to reach the global minimum, representing a solution of the optimization problem [15–17]. The *physical* strategy is to use a natural system or build a device whose physical ground state represents the sought-after solution [18–21]. In both cases, by progressively reducing the escape probability, the system is allowed to explore its configuration space and eventually "freeze" in the global minimum with some probability.

A. Quantum annealing Hamiltonian

The quantum annealing Hamiltonian is given by

$$H(t) = A(t)H_X + B(t)H_{\rm I}\,, \tag{1}$$

where $H_X = -\sum_i \sigma_i^x$ (with σ_i^x being the Pauli matrix acting on qubit i) is the transverse field, $H_{\rm I}$ is the classical Ising

[1] We note that phases of quantum models often have an accurate mean-field description, and that SQA is a classical simulation method obtained by mapping a quantum spin model to a classical one after the addition of an extra spatial dimension of extent β (the inverse temperature). Moreover, SQA scales polynomially in problem size, which is the reason that Ref. [7] was able to use SQA to predict the experimental outcomes of 108 qubit problem instances.

Hamiltonian,

$$H_{\rm I} = -\sum_{i\in\mathcal{V}} h_i\sigma_i^z - \sum_{(i,j)\in\mathcal{E}} J_{ij}\sigma_i^z\sigma_j^z\,, \qquad (2)$$

and the time-dependent functions $A(t)$ and $B(t)$ control the annealing schedule. Typically $A(t_f) = B(0) = 0$, where t_f is the total annealing time, and $A(t)$ [$B(t)$] decreases (increases) monotonically. The local fields $\{h_i\}$ and couplings $\{J_{ij}\}$ are fixed. The qubits occupy the vertices $\mathcal{V}$ of a graph $G = \{\mathcal{V}, \mathcal{E}\}$ with edge set $\mathcal{E}$.

A *spin configuration* is one of the 2^N elements of a set of ±1 eigenvalues of all the Pauli matrices $\{\sigma_i^z\}_{i=1}^N$, which we denote without risk of confusion by $\vec{\sigma}^z = (\sigma_1^z, \ldots, \sigma_N^z)$. The goal is to find the minimal energy spin configuration of $H_{\rm I}$, i.e., $\mathrm{argmin}_{\vec{\sigma}^z} H_{\rm I}$. In SA, this problem is solved by starting with a random initial spin configuration, flipping spins at random at each time step while always accepting a new spin configuration if it lowers the energy and accepting it probabilistically otherwise (using, e.g., the Metropolis rule), and gradually lowering the temperature to reduce the escape probability [15]. In QA, spin flips and the thermal escape rule are replaced by introducing the non-commuting field H_X [16, 17, 22, 23], which allows quantum tunneling out of local minima. The escape probability is reduced by turning off this non-commuting field adiabatically, i.e., the time-scale of the variation of the $A(t)$ and $B(t)$ functions must be slow compared to the inverse of the minimal energy gap of $H(t)$. In a physical device implementation of QA there is always a finite temperature effect, and hence one should consider both tunneling and thermal hopping [24–27].

Such physical QA devices, operating at $\sim 20\,\mathrm{mK}$ using superconducting flux technology, have been built by D-Wave [2–4]. The qubits occupy the vertices of the "Chimera" graph shown in Fig. 16 of Appendix A. Excluding the coupling to the thermal bath, the Hamiltonian driving the device is well-described by Eq. (1), with the functions $A(t)$ and $B(t)$ depicted in Fig. 1.

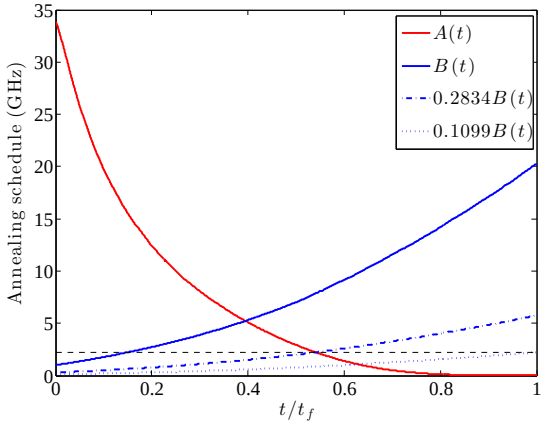

FIG. 1. DW2 annealing schedules $A(t)$ and $B(t)$ along with the operating temperature of $T = 17\mathrm{mK}$ (black dashed horizontal line). The large $A(0)/(k_BT)$ value ensures that the initial state is the ground state of the transverse field Hamiltonian. The large $B(t_f)/(k_BT)$ value ensures that thermal excitations are suppressed and the final state reached is stable. Also shown are the attenuated $\alpha B(t)$ curves for (a) the value of α at which the intersection between $A(t)$ and $\alpha B(t)$ coincides with the operating temperature (blue dot-dashed curve), and (b) the largest α such that $\alpha B(t)$ remains below the temperature line for the entire evolution (blue dotted curve).

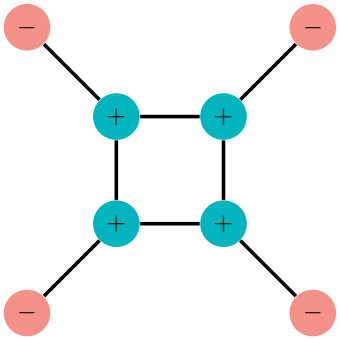

FIG. 2. The 8-spin Ising Hamiltonian. The inner "core" spins (green circles) have local fields $h_i = +1$ [using the convention in Eq. (2)] while the outer spins (red circles) have $h_i = -1$. All couplings are ferromagnetic: $J_{ij} = 1$ (black lines).

B. The quantum signature Hamiltonian

Ref. [6] introduced an 8-qubit "quantum signature Hamiltonian," schematically depicted in Fig. 2, designed to distinguish between SA and QA. Specifically, subject to this Hamiltonian, SA and QA make distinct predictions concerning the ground state population distribution. Let us first briefly review the arguments leading to these distinct predictions.

The 8 spin problem comprises 4 spins connected in a ring, which we refer to as *core* spins, and 4 additional spins connected to each core spin, which we refer to as *outer* spins. One special property of this Hamiltonian is that it has a 17-fold degenerate ground state. Of these, 16 states form a closed subspace of spin configurations connected via single flips of the outer spins, hence we refer to them as the *clustered* (C) ground states, or just the "cluster-states", or "cluster". There is one additional state, which we call the *isolated* (I) ground state, connected to the cluster-states via 4 core spin flips:

$$\mathrm{C}: \{|0000\,0000\rangle, |0001\,0000\rangle, \ldots, |1111\,0000\rangle\}\,, \qquad (3a)$$

$$\mathrm{I}: \{|\underbrace{1111}_{\text{outer}}\,\underbrace{1111}_{\text{core}}\rangle\}\,, \qquad (3b)$$

where $|0\rangle$ and $|1\rangle$ are, respectively, the $+1$ and -1 eigenstates of σ^z. This structure of the ground state manifold is easily verified by inspection of the Hamiltonian of Fig. 2.

The clustered ground states arise from the frustration of the outer spins, due to the competing effects of the ferromagnetic coupling and local fields. This frustration arises only when the core spins have eigenvalue $+1$, which is why there is only a single additional (isolated) ground state where all spins have

eigenvalue -1 (for a more detailed discussion of the energy landscape of this 8-spin Hamiltonian, see Ref. [6].) Here we also consider quantum signature Hamiltonians with larger numbers of spins N, as depicted in Fig. 3. These Hamiltonians share the same qualitative features, but the degeneracy of the ground state grows exponentially with N:

$$\begin{aligned} \text{Degeneracy of C}: &\quad N_{\rm C} = 2^{N/2}\,; \\ \text{Degeneracy of I}: &\quad N_{\rm I} = 1\,. \end{aligned} \tag{4}$$

Let us denote the probability of the isolated state at $t = t_f$ by $P_{\rm I}$, and the average probability of the population in the cluster at $t = t_f$ by $P_{\rm C} = \frac{1}{N_{\rm C}} \sum_{c=1}^{N_{\rm C}} P_c$, where $N_{\rm C} = 16$ for the 8-spin case, and where P_c is the probability of cluster-state number c. As shown in Ref. [6] for the 8-spin case, SA and QA can be distinguished because they give opposite predictions for the population ratio $P_{\rm I}/P_{\rm C}$. The same arguments can be straightforwardly generalized to the $N > 8$ cases, as we show in detail in Appendix B 1; here we briefly review the qualitative argument.

In the case of QA, $P_{\rm I}/P_{\rm C}$ is less than or equal to 1, meaning that the isolated state is suppressed relative to the average population in the cluster-states. This can easily be explained as follows. If we denote the instantaneous ground state of the system along the annealing schedule by $|0_t\rangle$, then one can show by exact diagonalization (see Appendix B 2) that it has vanishing support on the isolated state towards the end of the annealing protocol:

$$\langle {\rm I}\,|\,0_t\rangle = 0, \quad t \to t_f\,. \tag{5}$$

As a consequence, ideal QA evolution (i.e., closed system evolution satisfying the adiabatic condition) would yield a vanishing population in the isolated state, $P_{\rm I} = 0$. However, deviations from adiabaticity, or coupling to a thermal environment, can populate excited states with support on the isolated state, which results in $P_{\rm I} > 0$. As long as these non-idealities are sufficiently small the isolated state population will remain suppressed relative to the average population of the cluster-states. For this reason, we say that for QA, the isolated state is *suppressed* relative to the cluster-states.

In contrast, $P_{\rm I}/P_{\rm C}$ is greater than or equal to 1 for a SA protocol, meaning that the isolated state population is *enhanced* relative to the average population of the cluster-states. This prediction can easily be explained in terms of simple thermalization effects involving only the ground and first excited states. Since the isolated state is connected via single spin flips to more excited states than the cluster-states, thermal fluctuations "feed" the former with a higher rate than the latter. Therefore, if SA is initialized in a randomly chosen initial state, there is a greater likelihood that the system will end up in the isolated state at the end of the protocol.

These two starkly different predictions for QA and SA allowed Ref. [6] to rule out SA as an explanation of the experimental results obtained from the DW1 using the 8-spin Hamiltonian. In addition, Ref. [6] demonstrated that the ME [11] correctly predicts the suppression of the isolated state, including the dependence on the annealing time t_f, thus providing evidence that the DW1 results correlate well with the predictions of open system quantum evolution. However, as we shall discuss in detail and demonstrate with data from the DW2, the suppression of the isolated state can change as a function of the thermal noise, and suppression can turn into enhancement at sufficiently high noise levels. Yet, this does *not* imply that the system admits a classical description.

III. TUNING THE THERMAL NOISE

The QA and SA protocols represent two opposite extremes: in the former quantum fluctuations dominate while in the latter thermal fluctuations dominate. Can we interpolate between these regimes on a physical annealer? Since we are unable to directly change the temperature on the DW2 device[2], our strategy to answer this question is to indirectly modify the relative strength of thermal effects during the annealing process. We shall argue that this can be done using three different parameters that are at our disposal: an overall energy scale, the total annealing time, and the number of spins.

A. Decreasing the energy scale α

A straightforward way to tune the thermal noise indirectly is to change the overall energy scale of the problem Hamiltonian $H_{\rm I}$ by rescaling the local fields and couplings by an overall dimensionless factor denoted by α:

$$(J_{ij}, h_i) \;\mapsto\; \alpha\,(J_{ij}, h_i) \tag{6}$$

In the notation above, $\alpha = 1$ corresponds to implementing the largest allowed value of the physical couplings on the device (assuming $|h_{\rm max}| = |J_{\rm max}| = 1$ in dimensionless units). The scale of the transverse field H_X is not changed.

For SA, reducing α is tantamount to increasing the temperature. Since this does not change the energy spectrum, the earlier arguments for SA remain in effect, and we expect to have $P_{\rm I} \geq P_{\rm C}$ for all $\alpha > 0$ values. This is confirmed in our numerical simulations as shown below.

For QA, decreasing α from the value 1 has two main effects, as can be clearly seen in Fig. 4. First, the minimal gap between the instantaneous ground state and the 17-th excited state is reduced (the lowest 17 states become degenerate at the end of the evolution as explained previously). Since thermal excitations are suppressed by a factor of $e^{-\beta\Delta}$ (with $\beta = 1/k_B T$ the inverse temperature and Δ the energy gap), a reduction in the gap will increase the thermal excitation rate [11]. Second, reducing α delays the appearance of the minimal gap. This

[2] On-chip variability of the SQUID critical currents leads to uncertainty in both the qubit biases h and the qubit coupling strengths J. These uncertainties are calibrated out each time the chip is thermally cycled. The conditions required for optimum calibration are however temperature-dependent. We therefore conduct our experiments at a fixed operating temperature of 17 mK.

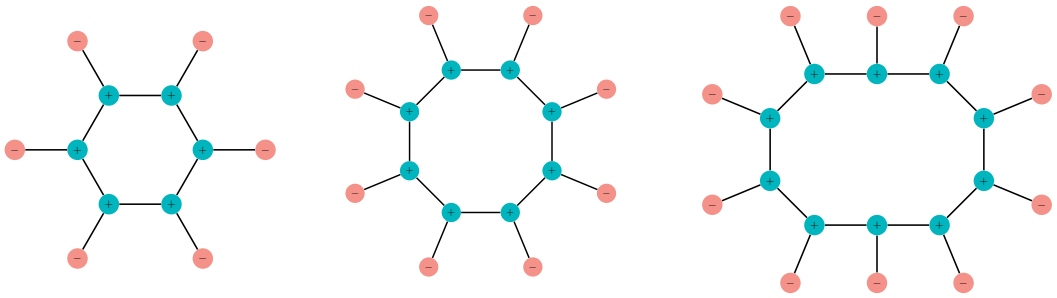

FIG. 3. Schematic representation of the 12, 16 and 20 spin Hamiltonians used in our tests. Extensions to larger N follow the same pattern, with $N/2$ qubits in the inner ring and $N/2$ qubits in the outer ring. Notation conventions are as in Fig. 2.

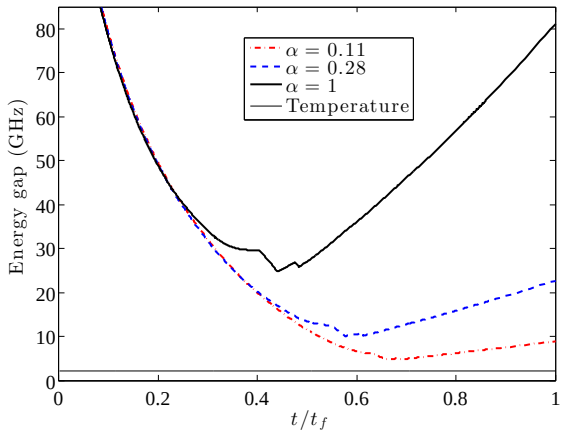

FIG. 4. Numerically calculated evolution of the gap between the instantaneous ground state and the 17-th excited state (which becomes the first excited state at $t = t_f$), for the 8-spin Hamiltonian in Eq. (1), following the annealing schedule of the DW2 device (Fig. 1). The gap value is shown for some interesting values of α (see Section IV). The kinks are due to energy level crossings, as explained in Appendix C. A reduction in α results in a reduction of the size of the minimal gap and delays its appearance.

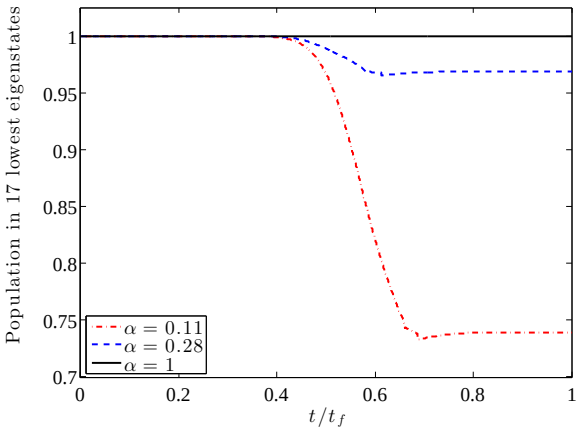

FIG. 5. ME simulation for the time-dependence of the probability of being in the lowest 17 energy eigenstates, for different values of α. Simulation parameters are $t_f = 20\,\mu s$ (the minimal annealing time of the DW2) and $\kappa = 1.27 \times 10^{-4}$, where κ is an effective, dimensionless system-bath coupling strength defined in Eq. (D6). The chosen value of κ allows us to reliably probe the small α regime.

effectively prolongs the time over which thermal excitations can occur, thus also increasing the overall loss of ground state population. Hence we see that by changing α we expect to move from a regime where thermal fluctuations are negligible ($\alpha \simeq 1$), to a regime where they are actually dominant ($\alpha \lesssim 0.1$), when the minimal gap is comparable to or even smaller than the physical temperature of the device.

In agreement with these considerations, the effect that the position and size of the minimal gap have on the probability of being in a given energy eigenstate is shown in Fig. 5. This figure shows the total population of the 17 lowest energy eigenstates (i.e., the subspace that eventually becomes the ground state manifold), computed using the ME described in Appendix D 1. As is clear from Fig. 5, as α decreases, the increasingly delayed and smaller gap causes this subspace to lose more population due to the increased rate and duration of thermal excitations. This behavior is interrupted by kinks caused by level crossing, whose position is a function of α, with the kinks occurring later for smaller α (see Appendix C).

B. Increasing the total annealing time t_f

As reported in Ref. [6] (which only studied the $\alpha = 1$ case), increasing the annealing time reduced the suppression of the isolated state, which is consistent with the effect of increased thermal excitations. To understand this, note that in general the requirement of high ground state fidelity generates a competition between adiabaticity (favoring long evolution times) and suppression of thermal effects (favoring short evolution times) [26]. Since the shortest annealing time of the DW2 ($20\mu s$) is already much longer than the inverse of the minimal gap ($\sim (25\,\mathrm{GHz})^{-1}$ at $\alpha = 1$; see Fig. 4), increasing the annealing time does not suppress non-adiabatic transitions, but does increase the probability of thermal fluctuations. One might expect that, by sufficiently reducing α, it is possible to make the gap small enough that the competition between adiabaticity and thermalization becomes important. However,

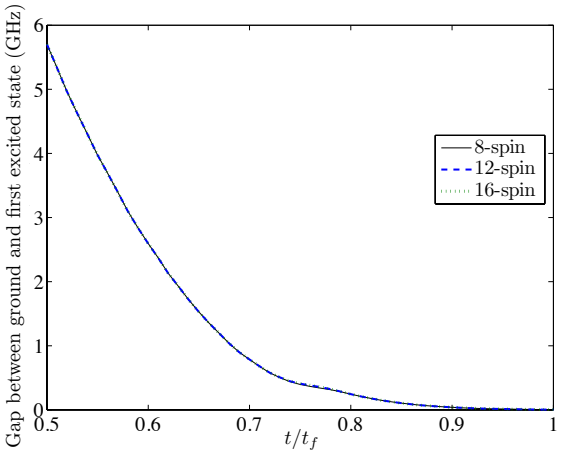

FIG. 6. Numerically calculated instantaneous energy gap between the ground and first excited state for the 8, 12 and 16 spin Hamiltonians. The gap vanishes since the first excited state becomes part of the $2^{N/2}+1$-fold degenerate ground state manifold at $t = t_f$.

the simulations we performed for the closed system case with $\alpha \in [0.01, 1]$ show that $P_{\rm I}/P_{\rm C}$ is essentially 0 over the entire range. Therefore we do not expect non-adiabatic transitions to play a role over the entire range of α's we studied.

C. Increasing the number of spins N

There are two important effects to keep in mind when considering larger numbers of spins N (even). First, increasing the number of spins does not change our previous argument that the instantaneous ground state has vanishing support on the isolated state towards the end of the evolution [Eq. (5)]. We show this explicitly using first order perturbation theory in Appendix B 2. This means that we should still expect that $P_{\rm I}/P_{\rm C} < 1$ for QA, unless thermal excitations dominate. Second, the degeneracy of the instantaneous first excited state grows with N, while the energy gap to the ground state remains fixed with N. The latter is illustrated in Fig. 6. Consequently there is an enhancement of the thermal excitation rate out of the instantaneous ground state into the first excited state, eventually feeding more population into the instantaneous excited states that have overlap with the isolated state. Thus we expect $P_{\rm I}/P_{\rm C}$ to grow with N (as we indeed find experimentally – see Fig. 10).

IV. EXPERIMENTAL RESULTS AND NUMERICAL SIMULATIONS

In this section we present our main experimental and numerical findings. In addition to testing the Hamiltonians described above for different values of α, t_f and N on the DW2, we have performed extensive numerical simulations using the master equation (ME), simulated annealing (SA), spin-dynamics (SD), and the hybrid model (SSSV), to determine the best model for the device at a finite temperature. Details about the numerical ME and SA simulations can be found in Appendix D. The SD and SSSV models are explained below. The data collection methodology is detailed in Appendix E. We note that our ME simulations have only one adjustable parameter, κ, an effective, dimensionless system-bath coupling strength defined in Eq. (D6). We present our findings by contrasting each of the classical models in turn with the experimental results, along with the ME simulations. We start with SA, followed by SD, and then SSSV, the latter being the new model that our results rule out.

A. Ruling out SA

1. *The 8-spin problem*

The main result showing the dependence of $P_{\rm I}/P_{\rm C}$ as a function of the energy scale α for $N = 8$ qubits is summarized in Fig. 7. We note first that the total ground state probability $P_{\rm GS} = P_{\rm I} + 16P_{\rm C}$ decreases monotonically as α is decreased. This reflects an increase in thermal excitations, whereby the ground state population is lost to excited states, and confirms that α acts as an effective inverse temperature knob.

However, in contrast to SA and in agreement with the ME, the DW2 result for $P_{\rm I}/P_{\rm C}$ is non-monotonic in α; see Fig. 7(a). Initially, as α is decreased from its largest value of 1, the ratio $P_{\rm I}/P_{\rm C}$ increases and eventually becomes larger than one, i.e., the population of the isolated state becomes enhanced rather than suppressed. A similar behavior is observed for the ME simulations but not for the SA simulations, as shown in Fig. 7(b). For sufficiently small α, the DW2 $P_{\rm I}/P_{\rm C}$ ratio turns around and decreases towards 1. Again, the same is observed for the ME simulation results. The SA results also converge to 1 as $\alpha \to 0$ but do not display a maximum. Therefore, we find a remarkable qualitative agreement between the DW2 data and the ME simulations over the entire range of α, whereas SA fails to capture the behavior of the $P_{\rm I}/P_{\rm C}$ ratio and can hence be ruled out, in agreement with earlier conclusions [6, 7]. [3,4]

In order to understand what contributes to the increase in $P_{\rm I}/P_{\rm C}$ as α is lowered, it is useful to study the time evolution of the population in the lowest 17 energy eigenstates

[3] The quantitative discrepancies between the ME and DW2 results can be attributed to the use of a weak system-bath coupling in the ME simulations. Using a larger system-bath coupling would increase thermal effects and result in a better match with the experimental results. However, computational resources limit our ability to explore larger values of the system-bath coupling, since this requires keeping track of more energy eigenstates in the simulations. The numerical results presented here are in a regime where the ME behaves reliably and can capture all the qualitative features of the DW2.

[4] A close examination of Fig. 7(a) shows that even in the "relatively classical" small α region ($\alpha \lesssim 0.1$) the curvature of $P_{\rm I}/P_{\rm C}$ for the DW2 matches that of the ME results ($d^2(P_{\rm I}/P_{\rm C})/d\alpha^2 < 0$) but is inconsistent with the curvature of the SA result ($d^2(P_{\rm I}/P_{\rm C})/d\alpha^2 > 0$), as seen in Fig. 7(b). We show in Appendix D 2 that the positive curvature of SA is a general result as long as the initial population is uniform.

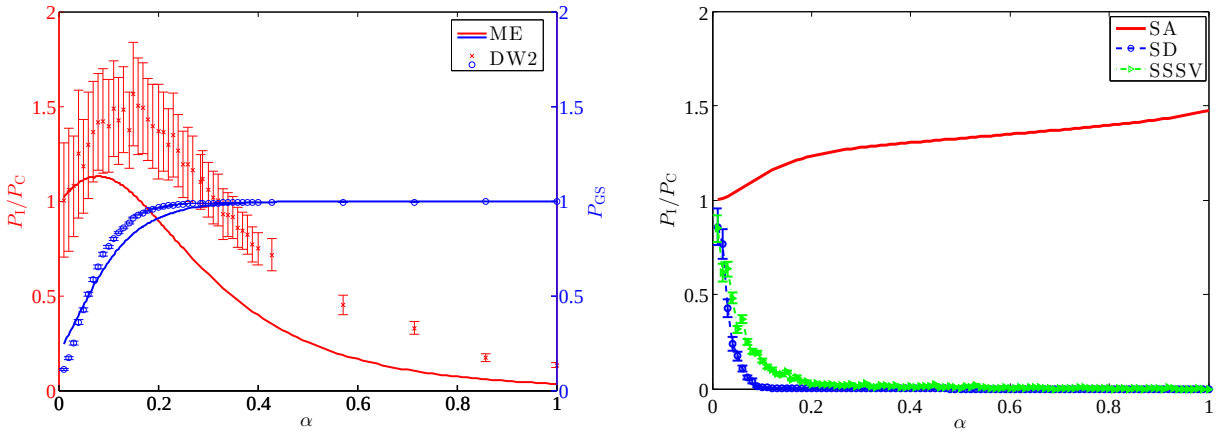

(a) (b)

FIG. 7. Experimental and numerical results distinguishing quantum and classical models for the DW2. (a) Experimental and ME results for the ratio of the isolated state population to the average population in the cluster-states ($P_{\rm I}/P_{\rm C}$), and the ground state probability ($P_{\rm GS}$), as a function of the energy scale factor α, at a fixed annealing time of $t_f = 20\,\mu s$. Two striking features are the "ground state population inversion" between the isolated state and the cluster (the ratio of their populations crosses unity), and the manifestly non-monotonic behavior of the population ratio, which displays a maximum. The $\times$ and $\circ$ symbols are the mean values of the bootstrapped [28] gauge-averaged distributions, and the error bars are one standard deviation below and above the mean. At the specific value of the system-bath coupling used in our simulations ($\kappa = 1.27 \times 10^{-4}$), the ME underestimates the magnitude and position of the peak in $P_{\rm I}/P_{\rm C}$ but qualitatively matches the experimental results, capturing both the population inversion and the presence of a maximum. (b) The population ratio and total ground state population as in (a), but from numerical simulations using the SA, SD, and SSSV models. In contrast to the ME results shown in (a), the SA, SSSV, and SD results for the population ratio are not in qualitative agreement with the experiment. Specifically, all three classical models miss the population inversion and maximum seen in (a). This suffices to reject all three as correct classical models of the D-Wave device. Simulation parameters can be found in Appendix D. Experimental data was collected using the in-cell embeddings strategy described in Appendix E. The embedding and gauge-averaging strategies are discussed in Sec. E 4.

according to the ME. An example is shown in Fig. 8, for $\alpha = 0.1$, i.e., close to the peak of the population ratio. This figure clearly shows how $P_{\rm I}/P_{\rm C}$ becomes > 1. The sixth energy eigenstate (red) evolves to become the isolated ground state, while the other 16 eigenstates evolve to become the cluster (purple). During the time evolution, the population in the sixth eigenstate grows slightly larger than that of the cluster (red curve ends up above the purple one), which explains why $P_{\rm I}/P_{\rm C} > 1$. In more detail, we observe that (around $t/t_f = 0.4$) the sixth eigenstate acquires population (via thermal excitations) from the lowest five eigenstates (blue). Somewhat later (around $t/t_f = 0.6$) the sixth eigenstate loses some population due to thermal excitations, which is picked up in part by the highest 11 eigenstates (green). Finally, thermal relaxation returns some population to the 17 eigenstates, but the sixth eigenstate gains more population than the other 16 eigenstates since it is connected to a larger number of excited states. During this relaxation phase, the system behaves like classical simulated annealing. The inset shows that deviations from the closed system behavior occur around $t/t_f = 0.4$, i.e., when the population of the sixth eigenstate first starts to grow (along with the highest 11 eigenstates) due to excitations from the lowest five eigenstates.

2. *Larger t_f*

Figure 9 shows that qualitatively similar results are observed when we increase the annealing time. As explained in Sec. III B, an increase in the annealing time is consistent with stronger thermalization, and indeed, over the range of α where we observe suppression of the isolated state ($P_{\rm I}/P_{\rm C} < 1$), this suppression is weaker for the larger total annealing time. The ME result is in qualitative agreement with the experimental data: the larger annealing time curve is the higher of the two, and the peak values of $P_{\rm I}/P_{\rm C}$ at the two different annealing times coincide, which also agrees with the experimental result, within the error bars.

3. *Larger N*

We have studied the simplest extensions beyond $N = 8$ (examples are shown in Fig. 3) with 12, 16 and 40 spins. As argued in Sec. III C, we expect the same qualitative features observed for $N = 8$ to persist. This is confirmed in Fig. 10, which displays the same qualitative non-monotonic behavior as a function of α. The main difference is that the enhancement of the isolated state (when $P_{\rm I}/P_{\rm C} > 1$) becomes stronger as N is increased. This is a manifestation of the growth, with N, in the number of excited states connected to the isolated

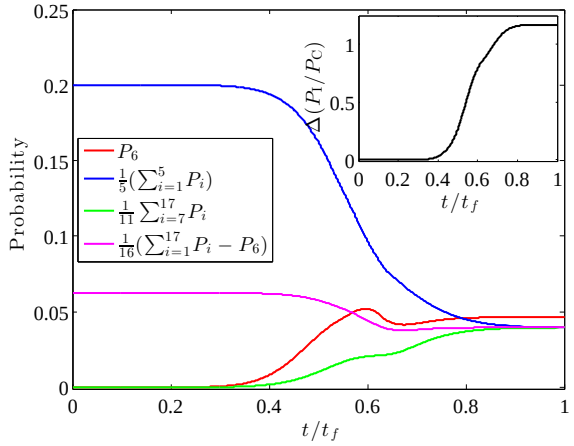

FIG. 8. Time evolution (according to ME) of energy eigenstate populations for $\alpha = 0.1$ and $\kappa = 8.9 \times 10^{-4}$ (this relatively large value was chosen here since it results in increased thermal excitation/relaxation). P_i denotes the population of the ith eigenstate, with $i = 1$ being the instantaneous ground state. The energy eigenstate that eventually becomes the isolated ground state is $i = 6$ (red). This state acquires more population at the end of the evolution than the other 16 eigenstates that eventually become the cluster (purple). Inset: The difference of the population ratio between the open system and the closed system evolution, $\Delta(P_1/P_C) = (P_1/P_C)_{\text{Open}} - (P_1/P_C)_{\text{Closed}}$. The deviation from closed system dynamics starts at $t/t_f \approx 0.4$, when the $i = 6$ eigenstate becomes thermally populated at the expense of the lowest five eigenstates.

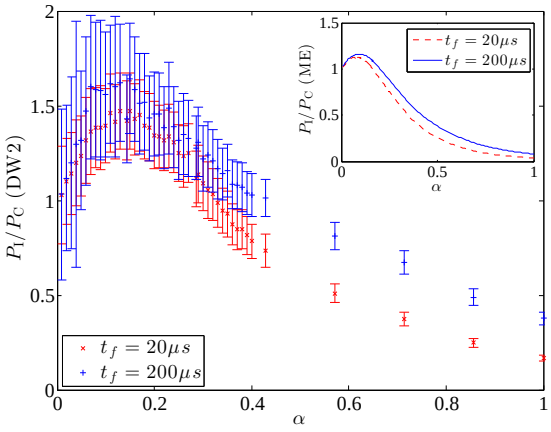

FIG. 9. Ratio of the isolated state population to the average population in the cluster (P_1/P_C) as a function of the energy scale factor α, for two different values of t_f, and $N = 8$. The inset shows the ME results. Data was collected using the "in-cell embeddings" strategy (see Appendix E 1 for details). The $t_f = 20\,\mu s$ data is the same as in Fig. 7(a).

state as compared to the number connected to the cluster-states. This, as explained in Sec. III C, implies that the excitation rate due to thermal fluctuations is proportionally larger for the isolated state than for the cluster-states.

B. Ruling out the SD model

In the O(3) spin-dynamics (SD) model, qubits are replaced by classical spins $\vec{M}_i = (\sin\theta_i \cos\phi_i, \sin\theta_i \sin\phi_i, \cos\theta_i)$. This is a natural semi-classical model since it amounts to the saddle-point approximation of the path integral for the spin system (the derivation is presented in Appendix F 1) and can be interpreted as describing coherent single qubits interacting classically. This model is closely related to one that was proposed and analyzed by Smolin & Smith [9] in its planar, O(2) version, i.e., $\vec{M}_i = (\sin\theta_i, 0, \cos\theta_i)$ (a spin in the $x-z$ plane). While the SD model was already shown to be inconsistent with the experimental data in the context of correlations with DW1 spin glass benchmarks in Refs. [7, 10], the SD model was shown in Ref. [9] to give the same suppression of the isolated state prediction as QA for $\alpha = 1$, and hence the evidence in Ref. [6] alone does not suffice to rule out the SD model as a classical description of the D-Wave device. In this subsection we shall demonstrate that similarly to SA, the SD model is also inconsistent with the experimental results we obtain when we tune the energy scale factor α of the quantum signature Hamiltonian.

As shown in Appendix F 2, the SD model with thermal fluctuations is described by a (Markovian) spin-Langevin equation [29, 30] with a Landau-Lifshitz friction term [30, 31],

$$\frac{d}{dt}\vec{M}_i = -\left(\vec{H}_i + \vec{\xi}(t) + \chi\vec{H}_i \times \vec{M}_i\right) \times \vec{M}_i \,, \qquad (7)$$

with the Gaussian noise $\vec{\xi} = \{\xi_i\}$ satisfying

$$\langle \xi_i(t) \rangle = 0 \,, \quad \langle \xi_i(t)\xi_j(t') \rangle = 2k_B T \chi \delta_{ij} \delta(t-t') \,, \qquad (8)$$

and

$$\vec{H}_i = 2A(t)\hat{x} + 2B(t)\left(h_i + \sum_{j\neq i} J_{ij}\vec{M}_j \cdot \hat{z}\right)\hat{z} \,, \qquad (9)$$

where $\hat{x}$ and $\hat{z}$ are unit vectors. For the nth run out of a total of N_r runs we obtain a set of angles $\{\theta_j^{(n)}\}$, which are interpreted in terms of a state in the computational basis by defining the probability of the $|0\rangle$ state for the jth spin (out of N) as $\cos^2(\theta_j^{(n)}/2)$. Therefore, we define:

$$P_C = \frac{1}{16N_r}\sum_{n=1}^{N_r}\prod_{j=N/2+1}^{N}\cos^2\left(\theta_j^{(n)}/2\right) \qquad (10a)$$

$$P_I = \frac{1}{N_r}\sum_{n=1}^{N_r}\prod_{j=1}^{N}\sin^2\left(\theta_j^{(n)}/2\right) \,, \qquad (10b)$$

where the product over the last $N/2$ spins in P_C is 1 if and only if all the core spins are in the $|0\rangle$ state, i.e., a cluster state, and likewise the product over all N spins in P_I is 1 if and only if all the spins are in the $|1\rangle$ state, i.e., the isolated state. To incorporate the α-dependence we simply rescale $B(t)$ to

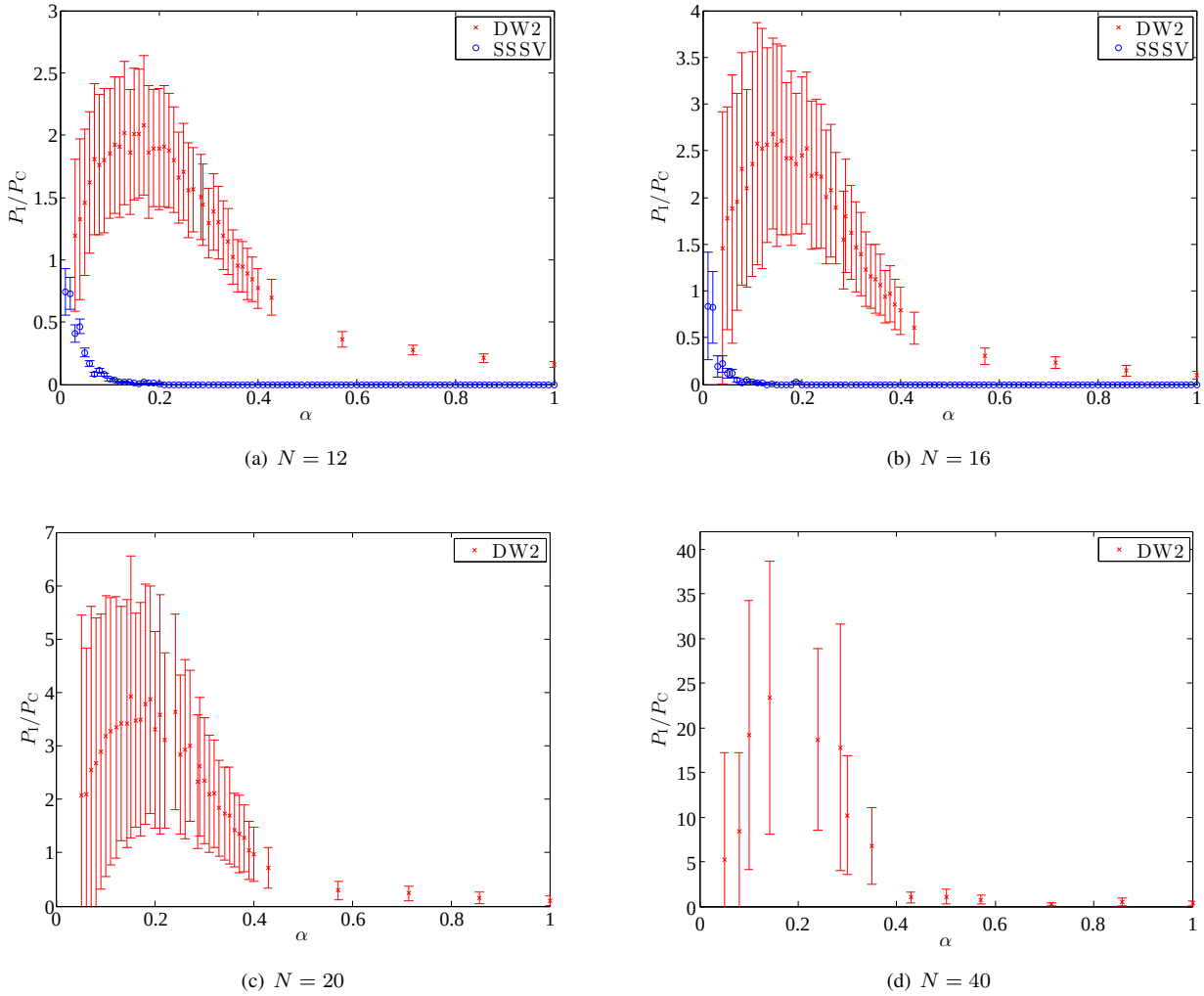

(a) $N = 12$ (b) $N = 16$

(c) $N = 20$ (d) $N = 40$

FIG. 10. Ratio of the isolated state population to the average population in the cluster-states (P_I/P_C) as a function of the energy scale factor α, for different values of N, at a fixed annealing time of $t_f = 20\,\mu s$. The non-monotonic dependence of the population ratio on α is observed for all values of N. The growth of the P_I/P_C peak with increasing N is consistent with the discussion presented in Sec. III C. The increasingly large error bars are due to the smaller amount of data collected as N grows. For $N = 12, 16, 20$ data was collected using the "random parallel embeddings" strategy and for $N = 40$ using the "designed parallel embedding" strategy (see Appendix E 1 for details). Also shown in each panel are the P_I/P_C values predicted by the SSSV model for $N = 12, 16$, at a fixed temperature 10.56 mK and 5×10^5 Monte Carlo step updates. For $N = 20, 40$, our simulations for SSSV model showed no deviation from zero despite taking more than 2.4×10^5 samples, so these results are not plotted. The SSSV model clearly does not match the experimental data.

$\alpha B(t)$.

Using the DW2 operating temperature and annealing schedules for $A(t)$ and $B(t)$, we find that the SD model does not match the experimental data. This can be seen in Fig. 7(b), where the SD population ratio (the dashed blue line) fails to reproduce the qualitative features of the DW2 result, in particular the ground state population inversion peak. Another illustration of the same failure of the SD model is given in Fig. 11, which shows the distribution of M^z for the core and outer qubits for different values of α. We expect the core spins to align in the $|1111\rangle$ state for sufficiently small α (i.e., to each have $M^z = -1$), when the isolated state becomes enhanced. However, as can be seen from Fig. 11 the median of the core spins is in fact never close to $M^z = -1$ for small α values, so that the enhancement of the isolated state is missed by the SD model. Furthermore, the model shows a preference for a particular cluster-state, the one with all of the outer spins in the $|1111\rangle$ state ($M^z = -1$). In the inset of Fig. 11, this can be seen in that the median of the data occurs always below $M^z = 0$. The explanation is provided in Appendix F 2.

Based on these discrepancies we find that the SD model can be ruled out as as model describing the quantum dynamics of the signature Hamiltonian. The Smolin-Smith model [9] is a related O(2) model and it shows the same behavior, so it is ruled out as well.

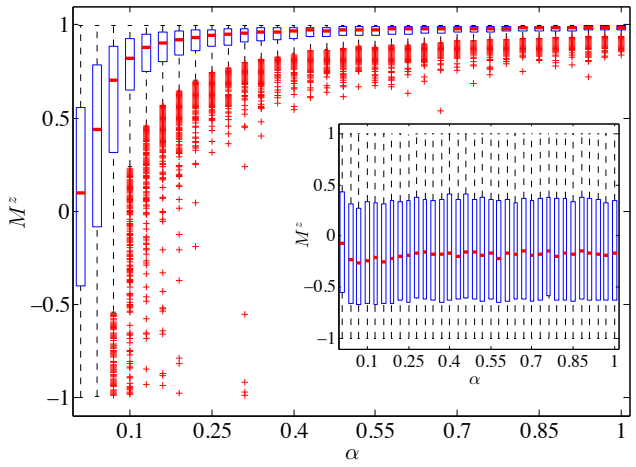

FIG. 11. Statistical box plot of the z component for all core qubits (main plot) and all outer qubits (inset) at $t = t_f = 20\mu s$. The red bar is the median, the blue box corresponds to the lower and upper quartiles, respectively, the dashed line contains most of the samples, and the $+$'s are outliers [32]. The data is taken for 1000 runs with Langevin parameters $k_B T/\hbar = 2.226\,\mathrm{GHz}$ (to match the operating temperature of the DW2) and $\chi = 10^{-3}$. In Appendix F 2 we show that the results do not depend strongly on the choice of χ.

C. Ruling out the SSSV model

Very recently a new hybrid of the O(2) model and SA was proposed [12]. This classical model presents a particularly interesting challenge since it nicely reproduces the success probability correlations that were used in Ref. [7] to reject SA and SD. Moreover, it accurately matches the quantum model used in Ref. [7] (SQA using quantum Monte Carlo) to provide evidence for quantum effects in the DW1 device, suggesting that the ground state population predictions of SQA relative to the random Ising instances used in Ref. [7] are almost identical to those of a classical mean-field approximation to SQA, namely the SSSV model. In this subsection we show that SSSV model in its original form fails to reproduce the qualitative features of the ground state population of our quantum signature Hamiltonian and therefore can also be rejected as a classical model of the D-Wave device.

The starting point of the SSSV model is a classical Hamiltonian inspired by the original QA model (1):

$$H(t) = -A(t)\sum_i \sin\theta_i + B(t)\left(-\sum_i h_i \cos\theta_i + \sum_{i,j} J_{ij}\cos\theta_i\cos\theta_j\right), \quad (11)$$

i.e., each qubit i is replaced by a classical O(2) spin $\vec{M}_i = (\sin\theta_i, 0, \cos\theta_i)$ and the annealing schedules $A(t)$ and $B(t)$ are the same as those of the D-Wave device. However, the time evolution is now governed by a Metropolis algorithm. In particular, at each discrete time step a certain number of Monte Carlo update steps are performed, as follows. Starting from the initial condition $\theta_i = \pi/2$, one variable at a time a random angle $\theta_i \in [0, \pi]$ is drawn with uniform probability. If this new angle does not increase the energy [as given by the Hamiltonian in Eq. (11)] it is accepted. If the new angle increases the energy it is accepted only if $p < \exp(-\beta\Delta E)$, where $p \in [0, 1]$ is drawn with uniform probability and $\Delta E > 0$ is the change in energy. Each complete time evolution following the entire annealing schedule constitutes one run. For the nth run out of a total of N_r runs we obtain a set of angles $\{\theta_j^{(n)}\}$, which is interpreted in terms of a state in the computational basis according to the sign of $\cos(\theta_j^{(n)})$, i.e., if $0 \le \theta_j^{(n)} \le \pi/2$ then it is the $|0\rangle$ state, whereas if $\pi/2 < \theta_j^{(n)} \le \pi$ then it is the $|1\rangle$ state.

To test whether this model matches the results of our quantum signature Hamiltonian we used the same parameters as given in Ref. [12], apart from the annealing schedule, for which we used that of the DW2. Ref. [12] found the best agreement with the DW1 data from Ref. [7] for a temperature of 10.6mK, lower than the 17mK operating temperature of the DW1, and for a total of 5×10^5 Monte Carlo update steps. We found negligible differences when we used the operating temperature of the DW2 for the SSSV model, or when we varied the number of Monte Carlo update steps. As can be seen in Fig. 7, the SSSV model does not reproduce the ground state population inversion and maximum seen in the experimental data. In fact the SSSV results are quantitatively similar to the SD model, even in showing a preference for a specific cluster-state (see Fig. 12). Furthermore, the SSSV model does not reproduce the ground state population inversion even after the number of qubits is increased to 40 (see Fig. 10(d), which is particularly significant as it shows that the essential quantum features that result in the disagreement are retained beyond the initial "small" $N = 8$ problem size. Based on these discrepancies the SSSV model can be rejected as a classical model for the D-Wave device.

These conclusions are robust to varying the two free parameters—the number of Monte Carlo step updates and the temperature—of the SSSV model. Decreasing the number of Monte Carlo updates or decreasing the temperature prevents the system from thermalizing and hence keeps the ratio of$P_{\mathrm{I}}/P_{\mathrm{C}}$ close to 0. Increasing the number of Monte Carlo updates or increasing the temperature has the reverse effect of thermalizing the system faster and pushing the ratio of $P_{\mathrm{I}}/P_{\mathrm{C}}$ towards 1. We have not found a mechanism—using only these two parameters—capable of selectively populating the isolated state to produce the experimentally observed ground state population inversion.

D. Modified SSSV models with strong or weak "decoherence" from O(2) rotors to Ising spins

The SSSV model captures the suppression of the isolated state at high α but fails to capture the ground state population

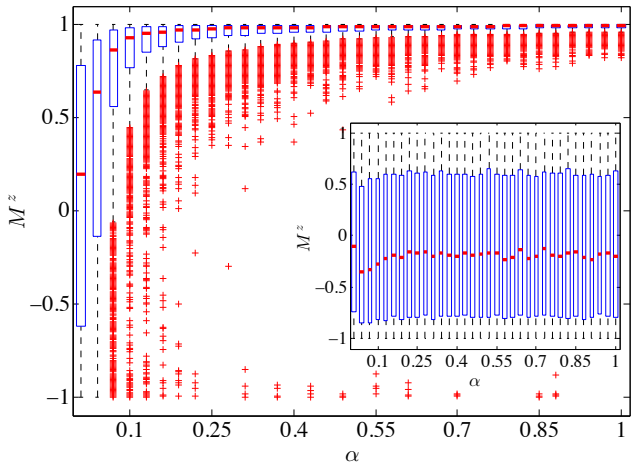

FIG. 12. Statistical box plot of the average z component for all core qubits (main plot) and all outer qubits (inset) at $t = t_f = 20\mu s$ for the SSSV model. The red bar is the median, the blue box corresponds to the lower and upper quartiles, respectively, the segment contains most of the samples, and the $+$'s are outliers [32]. The data is taken for 1000 runs with parameters $k_B T/\hbar = 1.382\,\mathrm{GHz}$ and 5×10^6 metropolis update steps per qubit. The time steps are discretized in steps of 10^{-3}.

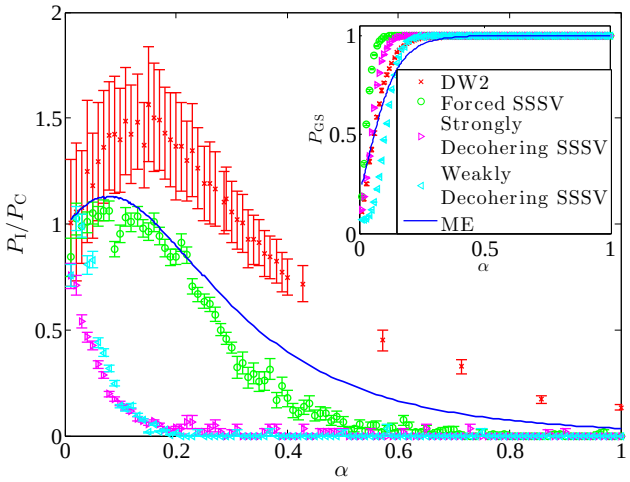

FIG. 13. "Forced" and strongly or weakly "decohering" SSSV models (Sections IV D and IV E). Shown are the results for the ratio of the isolated state population to the average population in the cluster-states (P_1/P_C) as a function of the energy scale factor α, for $N = 8$ and at a fixed annealing time of $t_f = 20\,\mu s$. For reference the plot also includes the curves for the DW2 and ME from Fig. 7(a). Additional parameters for the modified SSSV models: a fixed temperature of 10.56 mK, 5×10^5 Monte Carlo step updates per spin, and $g^2\eta = 10^{-6}$ for the strongly decohered model and $g^2\eta = 2.5\times10^{-7}$ for the weakly decohered model.

inversion at low α. On the other hand, SA correctly predicts an enhanced isolated state at low α but fails to predict the suppression at high α. Thus, we are led to consider a classical model that interpolates between SSSV at high α and SA at low α.

An important difference between SA and SSSV is that in SA the qubits are replaced by fully incoherent, classical Ising spins, while in SSSV each qubit is replaced by a "coherent" O(2) rotor.[5] Therefore a natural way to interpolate between SSSV and SA is to "decohere" the O(2) rotors over an α-dependent timescale τ_α. How to do this precisely is a matter of judgement and fine-tuning, and here we consider two natural decoherence models, which attempt to phenomenologically capture the actual decoherence of the physical qubits in the device.

1. *Strongly decohering SSSV model*

We expect the qubits to become more incoherent as α becomes smaller, until in the limit of vanishing α they fully decohere and become Ising spins in the computational basis. To model this we replace the x-component of the magnetization vector of each spin by $M_i^x = e^{-t/\tau_\alpha} \sin\theta_i$ and leave the z-component unchanged, i.e., $M_i^z = \cos\theta_i$. This is equivalent to a model of single-qubit dephasing in the computational basis, via the mapping to the density matrix $\rho_i = \frac{1}{2} I + \vec{M}_i \cdot \vec{\sigma}$, where $\vec{M}_i = (M_i^x, 0, M_i^z)$ and $\vec{\sigma} = (\sigma_i^x, \sigma_i^y, \sigma_i^x)$. This can be visualized as a gradual squashing of the Bloch sphere (restricted to the $x-z$ plane) into an ellipsoid (ellipse) with major axis in the z-direction and a shrinking minor (x-)axis. It is also equivalent to replacing the transverse field amplitude $A(t)$ in Eq. (11) by $A(t)e^{-t/\tau_\alpha}$ while leaving the magnetization unchanged, i.e., decreasing the time-scale over which the transverse field plays a role.

Next we ensure that τ_α is monotonically increasing with α. In this manner, for $t \ll t_f$ the range is almost that of the fully "coherent" SSSV, while for $t \lesssim t_f$ the range is restricted to that of the "incoherent" SA. The "decoherence" time τ_α dictates how quickly this transition from one extreme to the other occurs, and to incorporate its α-dependence we set $\tau_\alpha = 1/2\gamma_\alpha(0)$, where $\gamma_\alpha(0) = 2\pi g^2 \eta (\alpha\beta)^{-1}$ is the dephasing rate used in our ME calculations [the general expression for $\gamma(\omega)$ is given in Eq. (D5)], with a rescaled inverse temperature, i.e., $\alpha\beta$ instead of β, to capture the idea that α acts to rescale the energy, or equivalently the inverse temperature. Thus in this model $\tau_\alpha = \alpha \frac{\beta}{4\pi g^2 \eta}$. Note that we only replaced β by $\alpha\beta$ here and not anywhere else in the simulations, so the physical temperature is still given by β^{-1}.

Figure 13 presents the results of this "strongly decohering" SSSV model. The results are similar to the original SSSV model. Thus, "decoherence" of the coherent O(2) spins fails to improve the agreement with the experimental results, and the strongly decohering SSSV model can also be rejected

[5] Recall that SU(2) is (locally) isomorphic to SO(3), so a qubit can always be mapped to an SO(3) rotor. (Strictly, SO(3) is isomorphic to SU(2)/Z_2.) The restriction to O(2) rotors is not problematic since our QA Hamiltonian contains only x and z components.

on the basis of our experiments. Since the strongly decohered SSSV model implements "decoherence" of the individual O(2) spins in the same manner as predicted by the singular coupling limit ME [6], we can conclude that this type of strong system-bath coupling is not an appropriate model of the D-Wave device.

2. *Weakly decohering SSSV model*

We can consider a weaker version of this dephasing model, which attempts to mimic dephasing in the energy eigenbasis of the ME model. When the transverse field Hamiltonian dominates over the Ising Hamiltonian, the dephasing occurs in the z-component of the magnetization, and when the Ising Hamiltonian dominates over the transverse field Hamiltonians, the dephasing occurs in the x-component of the magnetization. Explicitly, this translates to replacing the magnetization components of the spin by

$$M_i^x = \sin\theta_i \ , \ M_i^z = e^{-t/\tau_\alpha}\cos\theta_i \ , \tag{12}$$

if $A(t) \geq \alpha B(t)$ and by

$$M_i^x = e^{-(t-t_c)/\tau_\alpha}\sin\theta_i \ , \ M_i^z = e^{-t_c/\tau_\alpha}\cos\theta_i \ , \tag{13}$$

if $A(t) < \alpha B(t)$, where t_c is the transition time satisfying $A(t_c) = \alpha B(t_c)$. As can be seen in Fig. 13, this model also fails to capture the experimental results.

E. A modified SSSV model with a forced transition from O(2) rotors to Ising spins

To try to get better agreement of a classical model with the experiment we finally consider a somewhat contrived model which simply forces a transition to SA with Ising spins. To implement this, instead of uniformly drawing $\theta_i \in [0, \pi]$ as in the SSSV model, we draw $\theta_i \in [0, \frac{\pi}{2}e^{-t/\tau_\alpha}] \cup [\pi - \frac{\pi}{2}e^{-t/\tau_\alpha}, \pi]$, where τ_α is selected just as in the decohered SSSV model (Section IV D). This can be visualized as a restriction of the range of angles to gradually shrinking top and bottom parts of the Bloch sphere (again restricted to the $x-z$ plane). We call this a "forced" SSSV model since it does not originate from a natural model of decoherence.

Figure 13 also presents the results of this "forced" SSSV model. In contrast to the SSSV model result [Fig. 7(b)], the population ratio now rises to 1 for $\alpha > 0$, in fact close to $\alpha = 0.2$ where $P_{\rm I}/P_{\rm C}$ peaks in the DW2 data. In this regard the "forced" SSSV model qualitatively captures the tendency toward ground state population inversion. However, it does not exhibit a pronounced ground state population inversion, and this appears to be a robust feature that is shared by other forced SSSV models we have tried (with different "forcing" rules).[6] Furthermore, it exhibits a noticeable drop in $P_{\rm I}/P_{\rm C}$ at $\alpha \approx 0.1$, and the fraction of ground state population is almost one in the ground state population inversion regime, in contrast to what is observed experimentally. In this sense even the "forced" SSSV model does not agree with the DW2 data, and further evidence to this effect is presented in the next subsection (Section IV F). Still, we cannot rule out that further fine-tuning of the "forcing" rule might eventually reproduce all the ground state features.

[6] In fact the same plateau ($P_{\rm I}/P_{\rm C} \approx 1$) is seen also in SQA simulations [33].

F. Distance from the Gibbs state distinguishes the classical and quantum models

How well does the system thermally equilibrate? In this section we consider how distinguishable the final density matrix $\rho(t_f)$ is from the thermal Gibbs state at t_f, using the standard trace-norm distance measure [34]

$$\mathcal{D}\left(\rho(t_f), \rho_{\rm Gibbs}\right) = \frac{1}{2}\|\rho(t_f) - \rho_{\rm Gibbs}\|_1 \ , \tag{14}$$

where $\rho_{\rm Gibbs} = e^{-\beta H(t_f)}/\mathcal{Z}$ with $\mathcal{Z} = {\rm Tr}e^{-\beta H(t_f)}$ the partition function, and $\|A\|_1 \equiv {\rm Tr}\sqrt{A^\dagger A}$ (the sum of the singular values of the operator A). Note the fact that in the Gibbs state all ground states are equiprobable, so that $P_{\rm I}/P_{\rm C} = 1$. This simple observation helps to explain many of the experimental results.

The trace-norm distance result is shown in Fig. 14 for the experimental DW2 data, the ME, and the six classical models. We note first that the experimental data and the ME are once again in good qualitative agreement. Specifically, as α decreases, $\mathcal{D}$ first decreases, then increases, then decreases again. The position of the peak at $\alpha \approx 0.1$ roughly agrees with that of the experimental $P_{\rm I}/P_{\rm C}$ and ME peaks observed in Fig. 7(a). However, in contrast to this qualitative agreement between the DW2 data and the ME, with the minimum in $\mathcal{D}$ appearing in both, none of the six classical models exhibits a minimum at the corresponding value of α, thus confirming once more that they do not match the experimental data. This is particularly noticeable for the "forced" SSSV model, which as discussed above exhibited the best agreement with the *ground state* features among the classical models (Fig. 13), but poorly matches the excited state spectrum at low α, as can be inferred from Fig. 14. Indeed, this model is designed to transition to SA at low α, and it does so at $\alpha \approx 0.1$. It then deviates from SA at even lower α values, presumably since there is no transverse field at all in SA, but the transverse field remains active in the "forced" SSSV model at any $\alpha > 0$. Furthermore, we observe that the weakly decohering SSSV model has a higher trace-norm distance than all other models even at high α, and this is due to its strong preference for a particular cluster state, which is a failure mode of the SD and SSSV models that was discussed earlier.

Let us now focus on the DW2 results and explain the three regions seen in Fig. 14.

Large α, region (1): As α decreases from 1 to ≈ 0.3, since α is relatively large, thermal excitations are not strong enough to populate energy eigenstates beyond the lowest 17

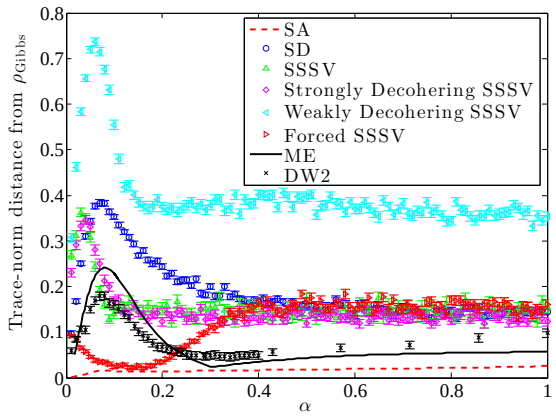

FIG. 14. Trace-norm distance of the DW2, ME, SA, SD, SSSV, weakly and strongly decohered SSSV, and forced SSSV states from the Gibbs state at $t_f = 20\,\mu s$ and $N = 8$. Three regions are clearly distinguishable for the DW2 and ME: (1) $1 \geq \alpha \gtrsim 0.3$, where $\mathcal{D}$ is decreasing as α decreases; (2) $0.3 \gtrsim \alpha \gtrsim 0.1$, where $\mathcal{D}$ is increasing as α decreases; (3) $0.1 \gtrsim \alpha \geq 0$, where $\mathcal{D}$ is again decreasing as α decreases. Both SA and SD lack the minimum at $\alpha \approx 0.3$. DW2 data was collected using the "in-cell embeddings" strategy (see App. E 1). For the DW2 results '$\circ$' gives the mean value of the bootstrapped gauge-averaged distributions and the error bars are one standard deviation below and above the mean (see App. E 2).

that eventually become the degenerate ground state. Therefore, the system is effectively always confined to the subspace that becomes the final ground state, as can also be seen from the $P_{\rm GS}$ data in Fig. 7(a). However, recalling that the isolated state has overlap with excited states higher in energy than the cluster-states for $t < t_f$ (see Appendix B 2), thermal excitations populate the isolated state. Thus as α decreases, $P_{\rm I}/P_{\rm C}$ approaches 1, which is also the ratio satisfied by the Gibbs state, and hence $\mathcal{D}$ decreases as observed. At the same time, Fig. 7(b) shows that at $\alpha = 0.3$ both the SD and SSSV models have $P_{\rm I}/P_{\rm C} \approx 0$, i.e., these models fail to populate the isolated state. This therefore suggests that the quantum spectrum makes it easier for the system to thermally hop from one eigenstate to another.

Intermediate α, region (2): Fig. 7(a) shows that $P_{\rm GS}$ begins to decrease from 1 at $\alpha \approx 0.3$, meaning that thermal excitations are now strong enough to populate energy eigenstates beyond the lowest 17. A loss in ground state population to excited states results, and the growth of $P_{\rm I}/P_{\rm C}$ beyond 1 seen in Fig. 7(a) results in the increase of $\mathcal{D}$ observed in Fig. 14. At $\alpha \approx 0.1$, the maximum distance from the Gibbs state is reached. Beyond this value of α, the energy scale of the Ising Hamiltonian is always below the temperature energy scale, as shown in Fig. 1.

Small α, region (3): As $\alpha \to 0$ there is only a transverse field left, which is gradually turned off. Thus the system approaches the maximally mixed state (which is the associated Gibbs state). In light of this, for $0.1 \gtrsim \alpha \geq 0$ the energy gaps are sufficiently small that there is a large loss of population from the ground state; thermal excitations become increasingly more effective at equilibrating the system, thus pushing it towards the Gibbs state.

G. Ground state entanglement during the course of the annealing evolution

Another way to address the question of the quantum nature of the evolution is to use the ME to compute an entanglement measure for the time-evolved state. Ground state entanglement was already demonstrated experimentally in Ref. [13] for a different Hamiltonian; here we are concerned with the time-dependent entanglement as a function of α, and are relying on the good qualitative match between the ME and our experimental results to justify this as a proxy for the actual entanglement. To this end we use the negativity (a standard measure of entanglement [35])

$$\mathcal{N}(\rho) = \frac{1}{2}\left(||\rho^{\Gamma_A}||_1 - 1\right) , \tag{15}$$

where ρ^{Γ_A} denotes the partial transpose of ρ with respect to a partition A. Figure 15 shows the numerically calculated negativity as a function of α along the time evolution for a "vertical" partition of the 8-qubit system, i.e., with an equal number of core and outer qubits on each side. Both the closed and open system evolution cases are shown. We observe that in the case of the closed system evolution there is always a peak in the negativity for all values of $\alpha \geq 0.01$ studied, with an α-dependent position. This is not surprising since as we change α, we change the relative position of the fixed ratio value of $A(t)/(\alpha B(t))$, and we expect the negativity peak to correspond to the position of the minimum gap of $H(t)$ [36].[7] For the open system case, in contrast, the negativity peak drops when α is sufficiently small. This can be said to signal a transition to classicality. The reason for this drop is that as α decreases the system thermalizes more rapidly towards the Gibbs state, but the Gibbs state is also approaching the maximally mixed state, which has vanishing entanglement. However, for large α the peak position and value is similar to that of the closed system case, so that the simulated system exhibits quantum features. This can be interpreted as another reason for the failure of all three classical models to reproduce the experimental data.

V. DISCUSSION

Motivated by the need to discern classical from quantum models of the D-Wave processor, we have introduced a new control knob—the energy scale of the final "quantum signature" Hamiltonian—that allowed us to thoroughly study the

[7] While this peak position does not precisely match the position of the minimum gap, the result in Ref. [36] holds in the thermodynamic limit and predicts a strict singularity; a discrepancy is therefore excepted in the case of a finite system size.

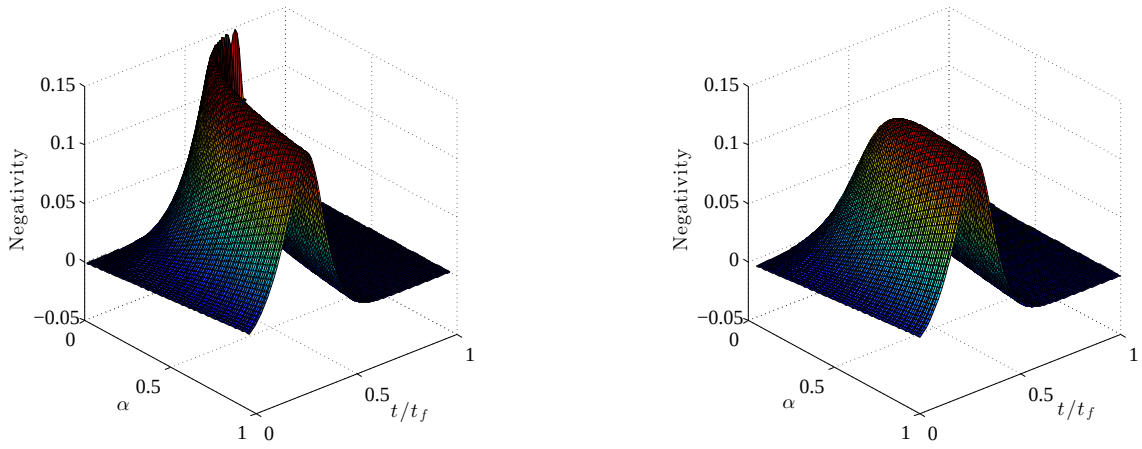

(a) Closed system

(b) Open system

FIG. 15. Time-dependence of the negativity [Eq. (15)] for (a) a closed system evolution and (b) an open system evolution of $N = 8$ qubits (modeled via the ME with $\kappa = 1.27 \times 10^{-4}$), as a function of α. The rapid decay of negativity for small α signals a transition to classicality. However, for large α the closed and open system negativity are similar, suggesting that the system is quantum in this regime. The apparent jaggedness of the closed system plot near $\alpha = 0$ is due to our discretization of α in steps of 0.01.

effect of thermalization on the annealing process realized with the D-Wave Two device. Lowering this energy scale acts as an effective temperature increase and thus enhances the effects of thermal fluctuations. Thermal excitations can also be enhanced by increasing the annealing time or by increasing the number of qubits, as thermal excitations are more probable when the duration of the coupling to the thermal environment is extended, or when the ground state subspace can couple to a larger number of excited states.

We have experimentally demonstrated the existence of two different regions in the energy scale where thermal fluctuations are either negligible or relevant. In the region where the relevant energy scale is much larger than temperature, the isolated ground state is suppressed, as expected in the case of quantum annealing. In the thermal region where the energy scale is comparable with or lower than the temperature, the isolated state population is enhanced (see Fig. 1). The same results are obtained for various annealing times and with Hamiltonians of up to 40 spins. As expected, thermal signatures are stronger when the annealing time or the number of spins are increased. Signatures of quantum annealing, on the other hand, remain strong even for the case of 40 spins.

The crucial finding of our work is that on the one hand the system is very well described by open system quantum dynamics along the entire energy scale, and on the other hand all of the classical models we have considered disagree with the experimental data for some portion of the energy scale, with one model ("forced" SSSV) coming close for the ratio of isolated to cluster ground state populations, but failing to agree for the distance from the total final state, which includes excited states. Moreover, the quantum model predicts that entanglement is generated along the evolution for sufficiently large values of the energy scale, while for small values entanglement rapidly vanishes, signaling a transition to classicality as the effective temperature becomes high enough. In this semiclassical region the system behaves similarly to a classical simulated annealer, (though even there we have found discrepancies with SA, i.e., in our experiments QA in the thermal region is neither a classical limit of QA nor is it SA). This observation can be of practical importance in the case of optimization problems where one expects that SA can be more efficient than QA [37]. In this case one might obtain a performance improvement by allowing the device to work in the thermal region. The possibility of such "thermally assisted" quantum annealing has been indeed demonstrated experimentally in [5], in the case of a specific toy problem. It is interesting to more generally characterize the (potentially beneficial) role played by thermal effects in affecting the performance of quantum annealing and adiabatic quantum computing [27, 38]. Apart from being a practical issue for the D-Wave device, thermal noise is a fundamental obstacle in determining the efficiency of any adiabatic algorithm [25, 26, 39]. This issue must be addressed by error correction [40], or by exploiting thermal noise as a computational resource [41].

VI. CONCLUSIONS

In this work we examined three previously published classical models of the D-Wave device (SA, SD [9], SSSV [12]), along with three new variants of the SSSV model with O(2) spins that transition to Ising spins, and found that all of these classical models are inconsistent with the experimental data in a "black-box" setting of a study of the input-output distribution of the device for a "quantum signature Hamiltonian." The SA and SD models were already rejected based on such inconsistency in earlier work [6, 7, 10] and the present evidence supports and strengthens these conclusions. The SSSV

model was of particular interest since it matches the input-output distribution of random Ising model experiments on the DW1 device [12]. While it is possible that with additional fine-tuning a better match can be achieved with a classical model, an adiabatic quantum master equation [11] we have examined is capable of reproducing all of the key experimental features with only one free parameter (the effective system-bath coupling κ). This bolsters the case for the importance of a quantum description of the input-output characteristics of the D-Wave device. It is important to stress that this master equation exhibits decoherence not in the computational basis but in the energy eigenbasis. Such decoherence is not a detriment to quantum annealing since it is consistent with maintaining computational basis coherence in the ground state.

The key evidence we have presented is the dependence of the ratio of populations in the isolated ground state and the cluster of ground states of the quantum signature Hamiltonian, as a function of the overall magnitude of this Hamiltonian (Figs. 7 and 10). The experiment and the quantum master equation display a non-monotonic behavior of this population ratio, while all three previously published classical models do not. One of variants of the SSSV model we have introduced ("forced" SSSV) comes close to the experimental result but it lacks a clear ground state population inversion, and more importantly, it does not match the experimental final state (Fig. 14). We have thoroughly analyzed and explained these findings. Our experiments cover the range of 8 to 40 qubits, extending beyond the unit cell of the D-Wave Two device.

How can the rejection of the classical SSSV model by our experimental data on quantum signature Hamiltonian problem instances of up to 40 qubits be reconciled with the conclusions of Ref. [12], which demonstrated a strong correlation between success probabilities of the SSSV model and the DW1 device for random Ising problem instances of 108 qubits? One obvious consideration is problem size, though Fig. 10 does not suggest that the agreement with experiment improves for the SSSV model as the number of qubits increases. More pertinent seems to be the fact that the quantum signature Hamiltonian experiment probes different aspects of the quantum annealing dynamics than the random Ising problem instances experiment. The former is, by design, highly sensitive to the detailed structure of the ground state degeneracy and the manner in which this degeneracy is dynamically generated, and these aspects are different for quantum and classical models. In this sense, it is a more sensitive probe than the random Ising experiment [7], which did not attempt to resolve the ground state degeneracy structure. While Ref. [12] established that the SSSV model correlates very well with the experimental success probability distribution for random Ising instances, and even better with SQA, our results suggest the possibility that a closer examination would reveal important differences between the SSSV model and QA also for the random Ising experiment. For example, Ref. [7] presented additional evidence for quantum annealing by also considering excited states and correlations between hardness and avoided level crossings with small gaps. Specifically, we conjecture that a detailed study of the ground state degeneracy for random Ising instances would determine the suitability of the SSSV model as a classical model for QA in this setting as well. Such a study might also circumvent an important limitation of our quantum signature Hamiltonian approach: the exponential degeneracy of the cluster states ($2^{N/2}$) makes gathering statistically significant data prohibitively time-consuming for $N > 40$. At the same time this exponential degeneracy can also be overcome by studying variants of our quantum signature Hamiltonian, e.g., with coupled outer qubits, and such studies are currently in progress.

We remark that we are, of course, aware that ruling out any finite number of classical models still leaves open the possibility that a new classical model can be found that explains the experimental data. Nevertheless, in the absence of a strict no-go test such as a Bell inequality violation, ruling out physically reasonable classical models while establishing close agreement with a quantum model (the adiabatic master equation), is a strategy that should bolster our confidence in the role played by quantum effects, even if it falls short of a proof that all classical models are inconsistent with the experiment.

Finally, we stress that the results reported here do not address the question of a quantum speedup on the D-Wave devices [42]. Such a question is of course meaningful only after a device has been demonstrated to display relevant quantum features and to defy a classical description, as this work suggests. Future work shall revisit this quantumness question using new tests and for larger system sizes.

ACKNOWLEDGMENTS

We would like to thank Gabriel Aeppli, Andrew Fisher, Andrew Green, and Matthias Troyer for valuable discussions. We thank Simone Severini for valuable discussions and a thorough and critical reading of an early version of the manuscript. Part of the computing resources were provided by the USC Center for High Performance Computing and Communications. This research used resources of the Oak Ridge Leadership Computing Facility at the Oak Ridge National Laboratory, which is supported by the Office of Science of the U.S. Department of Energy under Contract No. DE-AC05-00OR22725. The work of W.V. and P.A.W. has been done within a Global Engagement for Global Impact programme funded by EPSRC. The work of A.M., T.A. and D.A.L. was supported under ARO MURI Grant No. W911NF-11-1-0268, ARO grant number W911NF-12-1-0523, and the Lockheed Martin Corporation. AM was also supported by the USC Provost's PhD fellowship.

Appendix A: The D-Wave Two device

All our experiments were performed on the D-Wave Two (DW2) "Vesuvius" processor located at the Information Sciences Institute of the University of Southern California. Details of the device have been given elsewhere [2–4], and we only provide a brief overview here. As shown Fig. 16, the

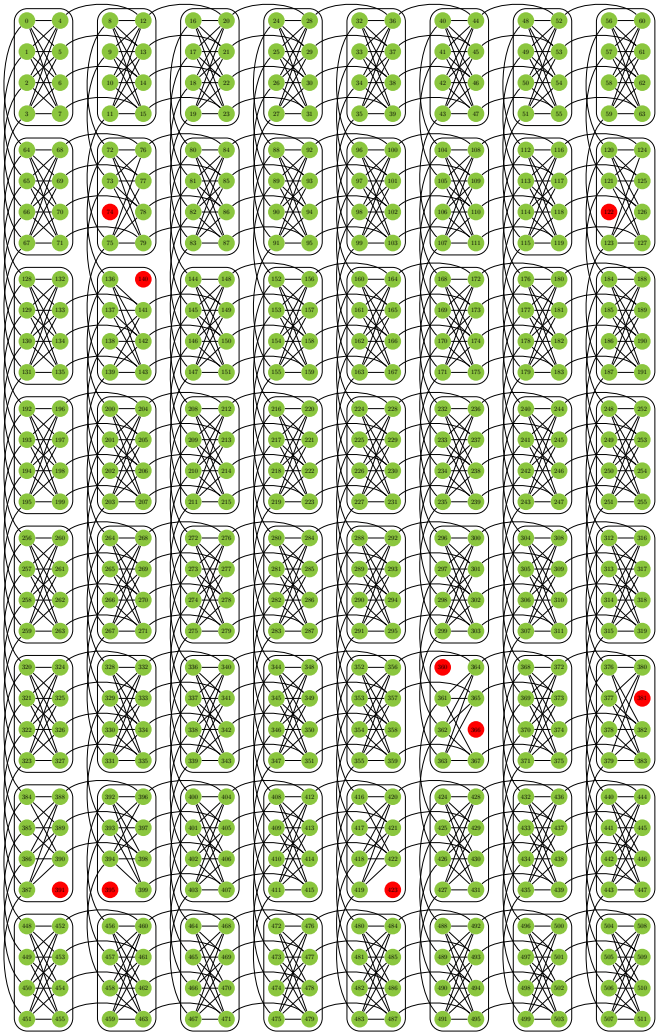

FIG. 16. **Qubits and couplers in the D-Wave Two device.** The DW2 "Vesuvius" chip consists of an 8×8 two-dimensional square lattice of eight-qubit unit cells, with open boundary conditions. The qubits are each denoted by circles, connected by programmable inductive couplers as shown by the lines between the qubits. Of the 512 qubits of the device located at the University of Southern California used in this work, the 503 qubits marked in green and the couplers connecting them are functional.

device is organized into an 8×8 grid of unit cells, each comprising eight qubits arranged in a $K_{4,4}$ bipartite graph, which together form the "Chimera" connectivity graph [43] of the entire device. Of the 512 qubits 503 were calibrated to within acceptable working margins in the DW2 processor used in our experiments. Figure 16 also gives a schematic representation of the most general problem Hamiltonian [as specified in Eq. (2)] that can be implemented in the device.

Appendix B: Enhancement *vs* suppression of the isolated state in SA *vs* QA

Here we review and generalize the detailed argument given in Ref. [6] for the enhancement of the isolated state in SA *vs* its suppression in QA.

1. Classical master equation explanation for the enhancement of the isolated state for general N

We first explain why SA predicts an enhancement of the isolated state for general (even) N. To do so we closely follow the arguments from Ref. [6] concerning the $N = 8$ case. Consider a signature Hamiltonian with $N = 2n$ qubits. As depicted in Fig. 3, n of these are the ferromagnetically coupled "core" qubits ($J_{ij} = 1$), while the other n "outer" qubits are each ferromagnetically coupled to a single core qubit ($J_{ij} = 1$). The local fields applied to the core qubits are $h_i = 1$, while $h_i = -1$ for the outer qubits.

Under our classical annealing protocol the system evolves via single spin flips. That is, at each step of the evolution a state can transfer its population only to those states which are connected to it by single spin flip. Thus the rate of population change in a state depends only on the number of states it is connected to via single spin flips. Let the index j run over all the states connected to state a; the Pauli master equation for the populations can then be written as

$$\dot{p}_a = \sum_j f(E_a - E_j)p_j - f(E_j - E_a)p_a, \tag{B1}$$

where we have assumed that the transfer function $f(\Delta E)$ does not depend on j and satisfies the detailed balance condition. For a derivation starting from the quantum master equation see Ref. [6] (Supplementary Information).

We shall now derive a classical rate equation for the generalization to N spins of the clustered and isolated states given in Eq. (3). Let $P_{\rm I}$ denote the population in the isolated state $|\underbrace{11\cdots1}_{n\text{ outer}}\,\underbrace{11\cdots1}_{n\text{ core}}\rangle$, and let $P_{\rm C} = 2^{-n}\sum_c P_c$ denote the average population of the cluster-states $\{|00\cdots0\,00\cdots0\rangle, \ldots, |11\cdots1\,00\cdots0\rangle\}$. For the isolated state, flipping either a core spin or an outer spin creates an excited state. An outer-spin flip changes the core-outer spin-pair from $|11\rangle$ to $|10\rangle$. This flip has an associated cost of 4 units of energy, and there are n such cases. A flip of one of the core qubits changes the core-outer spin-pair from $|11\rangle$ to $|01\rangle$. This results in two unsatisfied links in the core-ring, raising the energy by 4 units. However, the flip leaves the energy of the given core-outer spin-pair unchanged. There are again n such cases. Thus, for the isolated state, the rate equation is

$$\dot{P}_{\rm I} = 2n[f(-4)P_4 - f(4)P_{\rm I}] \tag{B2}$$

where P_4 is the population in the excited states which are 4 units of energy higher than the ground states.

The derivation of the rate equation for the cluster-states is somewhat more involved. We note first that a flip of any of the outer spins involves no energy cost, so all the excited states created from the cluster-states arise from flipping a core spin. Depending on the state of the outer spin when the core qubit is flipped, we have two different cases.

- If the outer is spin $|0\rangle$, the configuration of the core-outer pair changes from $|00\rangle$ to $|10\rangle$. This transition involves a change of 4 units of energy. Moreover, this creates a pair of unsatisfied links in the core-ring, at the cost of another 4 energy units. Overall, it takes 8 units of energy to accomplish this flip. To count the total number of such excited states connected to all cluster-states, let us consider a cluster-state with l outer spins in $|0\rangle$ and $n-l$ outer spins in $|1\rangle$. There are $\binom{n}{l}$ such cluster-states. In each of these states, we can choose any of the l core spins to flip. Thus, the overall number of all such possible excited states connected to cluster-states is $\sum_{l=0}^{n} l\binom{n}{l} = n2^{n-1}$.
- If the outer is spin $|1\rangle$, the configuration of the core-outer pair changes from $|01\rangle$ to $|11\rangle$. This core-outer transition involves no change of energy. However, this creates a pair of unsatisfied links in the core-ring, at a cost of 4 energy units. The counting argument for number of these excited states is same as in the previous case. Thus, the number of all such possible excited states connected to cluster-states is again $n2^{n-1}$.

We assume that all cluster-states have the same population, equal to the average population. The rate equation of the average cluster-states population is then

$$\dot{P}_{\rm C} = \frac{n2^{n-1}}{2^n}([f(-8)P_8 - f(8)P_{\rm C}] + [f(-4)P_4 - f(4)P_{\rm C}]) \tag{B3a}$$

$$= \frac{n}{2}\left[f(-8)P_8 - f(8)P_{\rm C} + f(-4)P_4 - f(4)P_{\rm C}\right], \tag{B3b}$$

where P_8 is the population in the excited states that are 8 units of energy above the ground states.

For most temperatures of interest, relative to the energy scale of the Ising Hamiltonian, the dominant transitions are those between the cluster and states with energy -4. Transitions to energy 0 states are suppressed by the high energy cost, and transitions from energy 0 states to the cluster-states are suppressed by the low occupancy of the 0 energy states.

$$\dot{P}_{\rm C} \approx \frac{n}{2}[f(-4)P_4 - f(4)P_{\rm C}] \tag{B4}$$

In classical annealing at constant low temperature starting from arbitrary states (that is, the high energy distribution), probability flows approximately $\dot{P}_{\rm I}/\dot{P}_{\rm C} \approx 4$ times faster into the isolated state initially, and it gets trapped there by the high energy barrier. To show that $\dot{P}_{\rm I} \geq \dot{P}_{\rm C}$ for slow cooling schedules, assume that this is indeed the case initially. Then, in order for $P_{\rm C}$ to become larger than $P_{\rm I}$, they must first become equal at some inverse annealing temperature β': $P_{\rm I}(\beta') = P_{\rm C}(\beta') \equiv P_g$, and it suffices to check that this implies that $P_{\rm I}$ grows faster than $P_{\rm C}$. Subtracting the two rate equations at this temperature yields

$$\dot{P}_{\rm I} - \dot{P}_{\rm C} = \frac{3n}{2}(f(-4)\,P_4 - f(4)\,P_g)$$
$$= \frac{3n}{2}f(-4)P_g\left(\frac{P_4}{P_g} - \frac{P(g\to 4)}{P(4\to g)}\right), \tag{B5a}$$

where in the second line we used the detailed balance condition, and $P(4\to g)$ denotes the probability of a transition from the excited states with energy 4 units above the ground state to the ground state g. Now, because the dynamical SA process we are considering proceeds via cooling, the ratio between the non-equilibrium excited state and the ground state probabilities will not be lower than the corresponding thermal equilibrium transition ratio, i.e., $\frac{P_4}{P_g} \geq \frac{P(g\to 4)}{P(4\to g)} = e^{-4\beta'}$. Therefore, as we set out to show,

$$\dot{P}_{\rm I} - \dot{P}_{\rm C} \geq 0\,, \tag{B6}$$

implying that at all times $P_{\rm I} \geq P_{\rm C}$.

2. Perturbation theory argument for the suppression of the isolated state in QA for general N

We consider the breaking of the degeneracy of the ground state of our N spin benchmark Ising Hamiltonian by treating the transverse field $H_X = -\sum_{i=1}^{N}\sigma_i^x$ as a perturbation of the Ising Hamiltonian (thus treating the QA evolution as that of a closed system evolving backward in time). As pointed out in the main text, the ground state is $2^{N/2}+1$-fold degenerate. According to standard first order degenerate perturbation theory, the perturbation $\hat{P}_g$ of the ground subspace is given by the spectrum of the projection of the perturbation H_X onto the ground subspace.

$$\Pi_0 = (|1\rangle\langle 1|)^{\otimes N} + (|0\rangle\langle 0|)^{\otimes N/2}(|+\rangle\langle +|)^{\otimes N/2}\,, \tag{B7}$$

where the first term projects onto the isolated state, and we have written the state of the outer qubits of the cluster in terms of $|+\rangle = (|0\rangle + |1\rangle)/\sqrt{2}$. We therefore wish to understand the spectrum of the operator

$$\hat{P}_g = \Pi_0\left(-\sum_{j=1}^{N}\sigma_j^x\right)\Pi_0\,. \tag{B8}$$

The isolated state is unconnected via single spin flips to any other state in the ground subspace, so we can write $\hat{P}_g$ as a direct sum of the 0 operator acting on the isolated state and the projection onto the space $\Pi_0' = \Pi_0 - (|1\rangle\langle 1|)^{\otimes N} =$

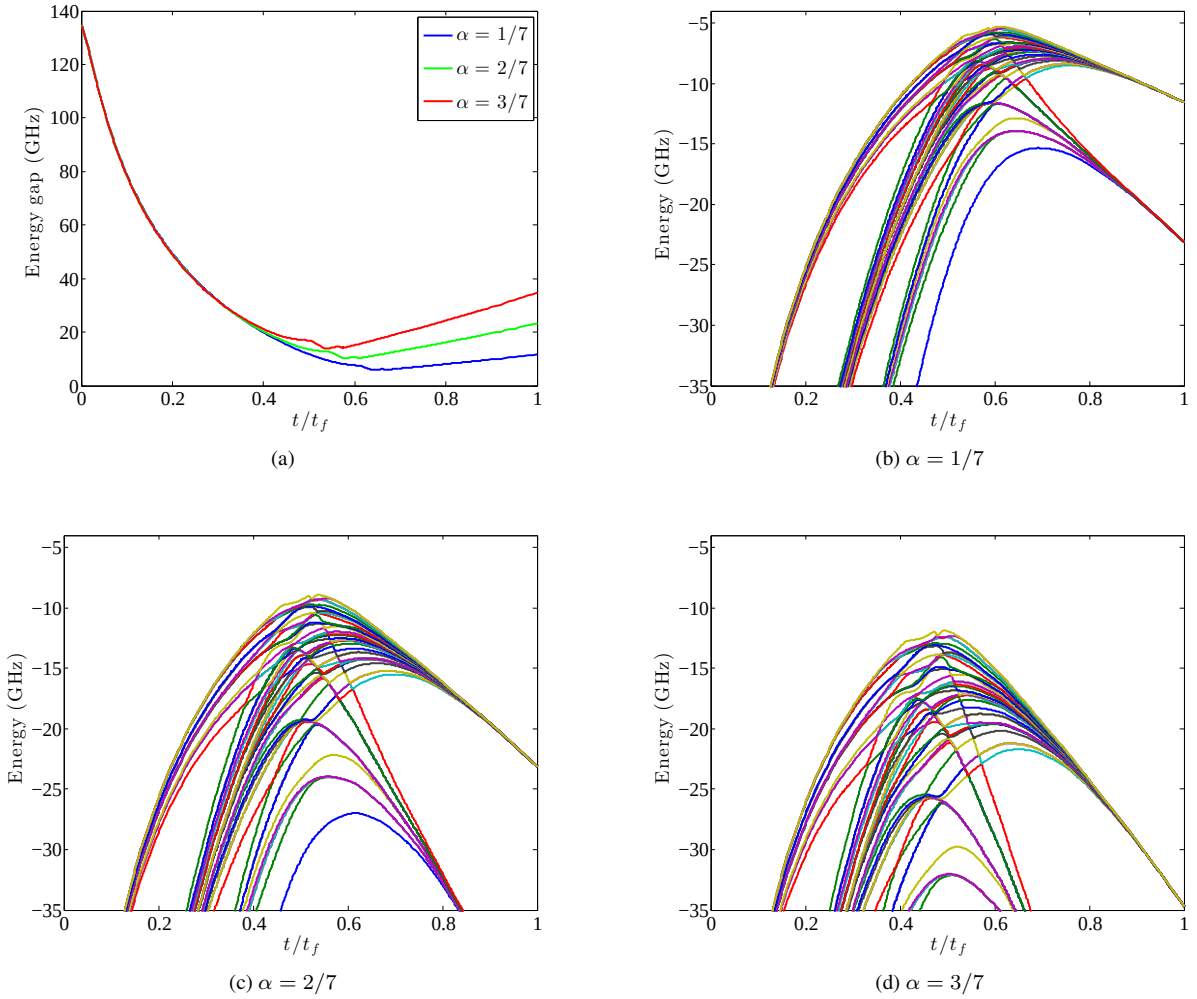

(a)

(b) $\alpha = 1/7$

(c) $\alpha = 2/7$

(d) $\alpha = 3/7$

FIG. 17. (a) Time-dependence of the gap between 18th excited state and the instantaneous ground state, for different values of the energy scale factor α. (b)-(d) Time-dependence of the lowest 56 energy eigenvalues for different values of α. Note that the identity of the lowest 17 energy eigenvalues changes over the course of the evolution.

$(|0\rangle\langle 0|)^{\otimes N/2}(|+\rangle\langle +|)^{\otimes N/2}$ of the cluster

$$\hat{P}_g = -0 \oplus \Pi_0' \left(-\sum_{j=1}^{N} \sigma_j^x \right) \Pi_0' \tag{B9a}$$

$$= -0 \oplus \left(-\sum_{j=N/2+1}^{N} \sigma_j^x \right) , \tag{B9b}$$

where the sum is over the outer qubits.

This perturbation splits the ground space of $H_{\rm I}$, lowering the energy of $|00\cdots 0++\cdots+\rangle$, and the $N/2$ permutations of $|-\rangle = (|0\rangle - |1\rangle)/\sqrt{2}$ in the outer qubits of $|00\cdots 0++\cdots+-\rangle$. None of these states overlaps with the isolated ground state, which is therefore not a ground state of the perturbed Hamiltonian. Furthermore, after the perturbation, only a higher (the sixth for $N = 8$) excited state overlaps with the isolated state. The isolated state becomes a ground state only at the very end of the evolution (with time going forward), when the perturbation has vanished. This explains why the isolated state is suppressed in a closed system model. A numerical solution of the ME agrees with this prediction for sufficiently large values of the problem energy scale α.

Appendix C: Kinks in the time dependence of the gap

Here we explain the origin of the kinks in the time dependence of the gap seen in Fig. 4. First, just as in Fig. 4 but for different values of α, we show in Fig. 17(a) how as α is decreased, the minimal gap occurs at a later time in the evolution and decreases in magnitude. The kinks that appear in both Fig. 4 and Fig. 17(a) are a consequence of energy level crossings apparent in the evolution of the spectrum, as shown in Fig. 17(b)-(d) for the same values of α as in Fig. 17(a). There are energy eigenstates that become part of the 17 degenerate

ground states that "cut" through other energy eigenstates.

Appendix D: Simulation details

1. Master Equation

We used an adiabatic Markovian master equation in order to simulate the DW2 as an open quantum system. Details of the derivation of the master equation can be found in Ref. [11]. The derivation assumes a system-bath Hamiltonian of the form:

$$H = H_S(t) + H_B + g\sum_\alpha A_\alpha \otimes B_\alpha \,, \tag{D1}$$

where A_α is a hermitian system operator acting on the αth qubit and B_α is a hermitian bath operator. We restrict ourselves to a model of independent baths of harmonic oscillators, i.e., each qubit experiences its own thermal bath, with a dephasing system-bath interaction,

$$A_\alpha = \sigma_\alpha^z\,; \quad B_\alpha = \sum_k \left(b_{k,\alpha} + b_{k,\alpha}^\dagger\right) \,, \tag{D2}$$

where $b_{k,\alpha}$ and $b_{k,\alpha}^\dagger$ are lowering and raising operators and k is a mode index. We use the double-sided adiabatic master equation *without* the rotating wave approximation [11]:

$$\begin{aligned}\frac{d}{dt}\rho_S(t) = &-i\left[H_S(t), \rho_S(t)\right] \\ &+ g^2 \sum_{\alpha\beta}\sum_{ab} \Gamma_{\alpha\beta}(\omega_{ba}(t))\left[L_{ab,\beta}(t)\rho_S(t), A_\alpha\right] \\ &+ \text{h.c.}\,,\end{aligned} \tag{D3}$$

where $\omega_{ba} = \varepsilon_b(t) - \varepsilon_a(t)$ are differences of instantaneous energy eigenvalues given by $H_S(t)\left|\varepsilon_a(t)\right\rangle = \varepsilon_a(t)\left|\varepsilon_a(t)\right\rangle$ and

$$L_{ab,\alpha}(t) = \left\langle\varepsilon_a(t)\right| A_\alpha \left|\varepsilon_b(t)\right\rangle \left|\varepsilon_a(t)\right\rangle\!\left\langle\varepsilon_b(t)\right| = L_{ba,\alpha}^\dagger(t)\,, \tag{D4a}$$

$$\begin{aligned}\Gamma_{\alpha\beta}(\omega) &= \int_0^\infty e^{i\omega t}\langle e^{-iH_B t} B_\alpha e^{iH_B t} B_\beta\rangle\, dt \\ &= \frac{1}{2}\gamma(\omega) + iS(\omega)\,,\end{aligned} \tag{D4b}$$

$$\gamma_{\alpha\beta}(\omega) = \int_{-\infty}^\infty \langle e^{-iH_B t} B_\alpha e^{iH_B t} B_\beta\rangle\, dt\,, \tag{D4c}$$

$$S_{\alpha\beta}(\omega) = \int_\infty^\infty d\omega' \gamma_{\alpha\beta}(\omega')\mathcal{P}\left(\frac{1}{\omega-\omega'}\right) d\omega'\,, \tag{D4d}$$

where $\mathcal{P}$ denotes the Cauchy principal value. Under the assumption of Ohmic independent baths, we have:

$$\gamma_{\alpha\beta}(\omega) = \delta_{\alpha\beta}\frac{2\pi g^2\eta\omega}{1-e^{-\beta\omega}} e^{-\omega/\omega_c}\,, \tag{D5}$$

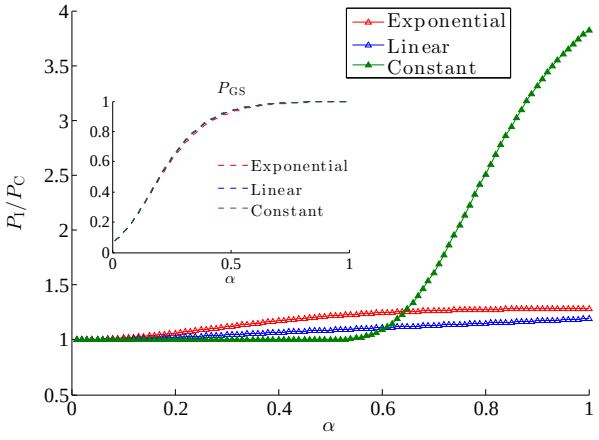

FIG. 18. Simulated annealing shows quantitatively similar behavior for various annealing schedule. The schedules are: exponential $T(k) = T(0)(T(K)/T(0))^{k/K}$, linear $T(k) = T(0) + \frac{k}{K}(T(K) - T(0))$, and constant $T(k) = T(K)$, with $K = 1000$, with $k_B T(0)/\hbar = 8$ GHz and $k_B T(K)/\hbar = 0.5$ GHz.

where β is the inverse temperature, η is a parameter (with units of time squared) characterizing the bath, and ω_c is an ultraviolet cut-off, which we set to 8π GHz to satisfy the assumptions made in deriving the master equation [11]. Note that the only remaining free dimensionless parameter is

$$\kappa \equiv g^2\eta/\hbar^2 \tag{D6}$$

(we have reintroduced the factor of $\hbar$ here), which controls the effective system-bath coupling. We choose to work with the master equation in Eq. (D3) instead of its counterpart in (completely positive) Lindblad form because it is numerically more efficient to calculate the evolution. Although it does not guarantee positivity of the density matrix, we always make sure to work in a parameter regime where we do not observe any violations of positivity.

2. Simulated Annealing

We describe here our implementation of classical simulated annealing. As the state of system at any given step is a classical probability distribution, we can represent it by a state vector $\vec{p}$, where the component p_i of the vector denotes the probability of finding the system in the ith state with energy E_i. We initialize in the maximally mixed state (infinite temperature distribution), i.e., $p_i = 1/2^N\ \forall i$. Note that the initial Gibbs state of the quantum annealer also has a uniform probability distribution over all computational states, so this choice for the classical initial state is well motivated. The system then evolves via single spin flips. The transition probability between two states with energy difference ΔE is given by $\frac{1}{N}\min(1, \exp(-\beta\Delta E))$, the Metropolis update rule [44].

The transition matrix has elements

$$\mathrm{T}(i \to j) = \frac{1}{N} \min(1, \exp(-\beta(E_j - E_i))) \,. \tag{D7}$$

The system is evolved for 1000 steps by acting with the transition matrix on the state vector $\vec{p}$. At each step, the temperature is adjusted so as to reduce thermal excitations. If the temperature is reduced slowly enough and to low enough energies, simulated annealing can find an optimal solution. The choice of temperature schedule to follow for simulated annealing is often motivated by experimental circumstances, and in the main text we used $\beta^{-1}B(t)$ (as shown in Fig. 1) as the schedule with $\beta^{-1}/\hbar = 2.226$ GHz. Here we tested three other different temperature schedules. As shown in Fig. 18, we find that the qualitative features of the simulation results do not depend on a particular choice of temperature schedule. While the numerical values of the ratio of the isolated state and cluster populations changes, the ratio is always greater than unity. The ground state population curves are indiscernible regardless of the temperature schedule used.

We can show that any SA protocol with a uniform initial state (corresponding to the infinite temperature Gibbs state) will give a positive curvature for the $P_{\mathrm{I}}/P_{\mathrm{C}}$ dependence on α around $\alpha = 0$. To see this, we expand the SA Markov-chain transition matrix in powers of α:

$$\mathrm{T}(\alpha) = \mathrm{T}_0 + \alpha \mathrm{T}_1 + \dots \,, \tag{D8}$$

where the SA state vector $\vec{p}(K)$ at the Kth time-step is given by $\vec{p}(K)^T = \vec{p}(0)^T \mathrm{T}(\alpha)^K$, where the T superscript denotes the transpose.

At $\alpha = 0$, all transitions are equally likely, so $(\mathrm{T}_0)_{ij} = 1/N$. The first order term satisfies:

$$(\mathrm{T}_1)_{i\to j} = \min\left(0, -\beta\left(E_j - E_i\right)\right) \,,\ i \neq j \,, \tag{D9a}$$

$$(\mathrm{T}_1)_{i\to i} = -\sum_j \min\left(0, -\beta\left(E_j - E_i\right)\right) \,. \tag{D9b}$$

The first order term has the property that $\sum_j (\mathrm{T}_1)_{ij} = 0$. Therefore, applying the transition matrix K times, we have to first order in α:

$$\vec{p}(K)^T = \vec{p}(0)^T (\mathrm{T}_0)^K + \alpha \vec{p}(0)^T \sum_{i=0}^{K-1} (\mathrm{T}_0)^{K-1-i} \mathrm{T}_1 (\mathrm{T}_0)^i + \dots \tag{D10}$$

Using the fact that we start from the uniform state $p_i(0) = 1/N$, we have $\vec{p}(0)^T \mathrm{T}_1 = 0$, but also that

$$(\mathrm{T}_1 \mathrm{T}_0)_{ij} = \frac{1}{N} \sum_k (\mathrm{T}_1)_{ik} = 0 \,. \tag{D11}$$

Therefore,

$$\vec{p}(K) = \vec{p}(0) + O(\alpha^2) \,. \tag{D12}$$

This in turn implies that for SA,

$$\frac{P_{\mathrm{I}}}{P_{\mathrm{C}}} = 1 + \alpha^2 f + O(\alpha^3) \,. \tag{D13}$$

Since we showed in Appendix B 1 that this quantity is greater than or equal to 1 for SA, this implies that $f \geq 0$, and hence the curvature $d^2(P_{\mathrm{I}}/P_{\mathrm{C}})/d\alpha^2$ at $\alpha = 0$ is positive.

However, we emphasize that this argument for the positivity of the initial curvature of $\frac{P_{\mathrm{I}}}{P_{\mathrm{C}}}$ requires that the initial state be uniform. If a non-uniform initial state is chosen, there will be a non-zero linear term in α for $P_{\mathrm{I}}/P_{\mathrm{C}}$, which prevents us from concluding anything about the curvature.

Appendix E: Experimental data collection methodology

Our data collection strategy was designed to reduce the effects of various calibration and control errors. In this Appendix section we explain the main sources of such errors and our methods for reducing them. These methods are distinct from, and complementary to other error correction methods, inspired by stabilizer codes, that have been previously proposed and implemented [40, 45].

Each time (programming cycle) a problem Hamiltonian is implemented on the DW2 device, the values of the local fields and couplings $\{h_i,\, J_{ij}\}$ are set with a Gaussian distribution centered on the intended value, and with standard error of about 5% [46]. To average out these random errors we ran several different programming cycles for the same problem Hamiltonian as described in subsection E 1. Differences among the individual superconducting flux qubits can contribute to systematic errors. To average out these local biases, we embedded our Hamiltonian multiple times in parallel on the device using different flux qubits, as also explained in subsection E 1. Furthermore, we implemented different "gauges", a technique introduced in Ref. [6]. A gauge is a given choice of $\{h_i,\, J_{ij}\}$; a new gauge is realized by randomly selecting $a_i = \pm 1$ and performing the substitution $h_i \mapsto a_i h_i$ and $J_{ij} \mapsto a_i a_j J_{ij}$. Provided we also perform the substitution $\sigma_i^z \mapsto a_i \sigma_i^z$, we map the original Hamiltonian to a gauge-transformed Hamiltonian with the same energy spectrum but where the identity of each energy eigenstates is relabeled accordingly. In total, there are 2^N different gauges for an N-spin problem. We averaged our data using different programming cycles, embeddings, and gauges, as explained in subsection E 2. In addition we checked for errors due to correlations between successive runs (subsection E 3) and found these to be negligible. Finally, we describe a new method for correcting control errors that exploits the knowledge that the degenerate cluster states should ideally have the same population (subsection E 4).

1. Data collection strategies

We used two different data collection strategies that resulted in perfectly consistent results.

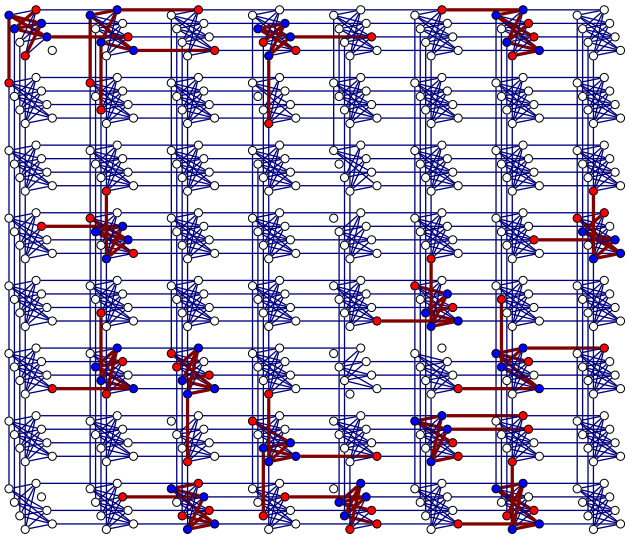

FIG. 19. Embedding according to the random parallel embeddings strategy for 8 spins. An example of 15 randomly generated different parallel copies of the 8-spin Hamiltonian. Our data collection used a similar embedding with 50 different copies.

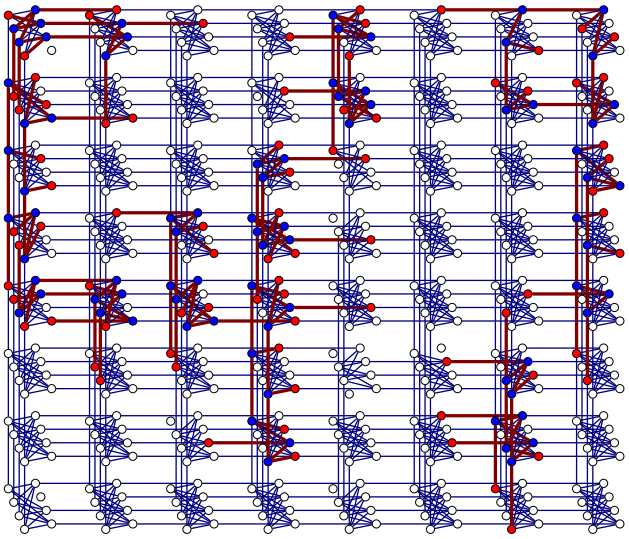

FIG. 20. Embedding according to the random parallel embeddings strategy for 16 spins. An example of 10 randomly generated different parallel copies of the 16-spin Hamiltonian. Our data collection used a similar embedding with 93 different copies.

Strategy A: Random parallel embedding. As illustrated in Fig. 19, 50 different parallel embeddings of the 8-spin problem Hamiltonian were generated randomly in such a way that an embedding is not necessarily limited to a unit cell. We thus solved 50 different copies of the same 8-spin problem in parallel during each programming cycle. We generated two such parallel embeddings containing 50 copies each. For each embedding, we performed 100 programming cycles and 1000 readouts for the runs with annealing time $t_f = 20\mu$s, 200μs; 200 programming cycles and 498 readouts for the runs with annealing time $t_f = 2000\mu$s; 500 programming cycles and 48 readouts for the runs with annealing time $t_f = 20000\mu$s. An example set of randomly generated embeddings for the 16 spin Hamiltonian is shown in Fig. 20.

Strategy B: In-cell embeddings. We utilized 448 qubits to program 56 parallel copies of the 8-spin problem Hamiltonian, with an identical gauge for all copies, with one copy per unit cell. All possible 256 gauges were applied sequentially. For a given annealing time t_f, the number of readouts was $\min(1000, \lfloor 5 \times 10^5/t_f \rfloor)$. For example, 1000 readouts were done for $t_f = 20\mu$s and 100 readouts for $t_f = 5000\mu$s. One such copy of an in-cell embedding is shown in Fig. 21. No in-cell embeddings are possible for problems involving $N > 8$ spins.

Strategy C: Designed parallel embedding. For $N = 40$, we utilized 320 qubits to program 8 parallel copies of the 40-spin problem Hamiltonian. The 40-qubit Hamiltonian was designed with three different embeddings spread across the Chimera graph. Each embedding occupied 6 different unit cells. 100 random gauges were chosen out of the 2^{40} possible

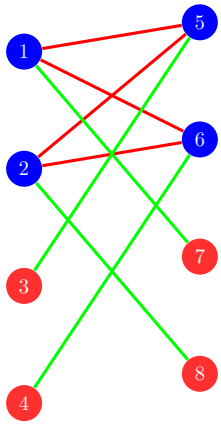

FIG. 21. Embedding according to the "in-cell embeddings" strategy. An example of a randomly generated in-cell embedding.

gauges and were identically applied to all 8 copies. To collect significant statistics, we performed 200 programming cycles with 10000 readouts for every gauge. The annealing time was $t_f = 20\mu$s.

2. Data analysis method

The following method was used to analyze the data. Let us denote the number of gauges by $N_{\rm G}$ and the number of embeddings by $N_{\rm E}$. For a given embedding a and gauge g, the number of total readouts (number of readouts times the num-

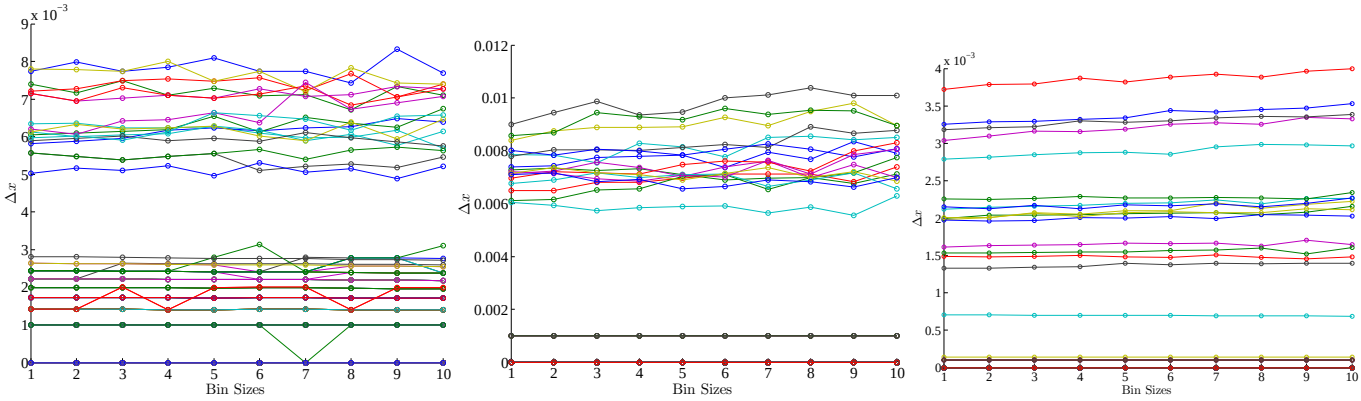

(a) $\alpha = 0.1$ (b) $\alpha = 0.35$ (c) $\alpha = 1$

FIG. 22. Some representative autocorrelation tests at $t_f = 20\mu s$ showing the standard error of the mean Δx as a function of binning size, for different values of α. Each curve is the result of the binning test for a different state. The relatively flat lines for all states suggest that there are no significant autocorrelations in the data.

ber of programming cycles) for the ith computational state is used to determine the probability $p_{a,g}(i)$ of that computational state. The gauge-averaged probabilities for the ith computational state $p_a^{\rm GA}(i)$ of the ath embedding are determined by averaging over the gauges for a fixed embedding:

$$p_a^{\rm GA}(i) = \frac{1}{N_{\rm G}} \sum_{g=1}^{N_{\rm G}} p_{a,g}(i) \,, \quad a = 1, \ldots, N_{\rm E} \,. \tag{E1}$$

Let us now consider a function of interest $\mathcal{F}$, for example $P_{\rm I}/P_{\rm C}$ or the trace-norm distance $\mathcal{D}(\rho_{\rm DW2}, \rho_{\rm Gibbs})$. Using the raw probabilities $p_{a,g}(i)$, we can calculate $\mathcal{F}_{a,g}$. For example, if $\mathcal{F} = P_{\rm I}/P_{\rm C}$, we have:

$$\mathcal{F}_{a,g} = \left(\frac{P_{\rm I}}{P_{\rm C}}\right)_{a,g} = \frac{16 p_{a,g}({\rm I})}{\sum_{i=1, i\in {\rm C}}^{16} p_{a,g}(i)} \,. \tag{E2}$$

For a fixed embedding a, we calculate the standard deviation $\sigma_a^{\rm G}$ associated with the distribution of $\mathcal{F}$ using the raw probabilities values over the $N_{\rm G}$ gauges, i.e.

$$\sigma_a^{\rm G} = {\rm std}\left[\{\mathcal{F}_{a,g}\}_{g=1}^{N_{\rm G}}\right] \,. \tag{E3}$$

For each embedding, we also calculate $\mathcal{F}_a^{\rm GA}$ using the gauge-averaged probabilities, e.g.,

$$\mathcal{F}_a^{\rm GA} = \left(\frac{P_{\rm I}}{P_{\rm C}}\right)_{a}^{\rm GA} = \frac{16 p_a^{\rm GA}({\rm I})}{\sum_{i=1, i\in {\rm C}}^{16} p_a^{\rm GA}(i)} \,. \tag{E4}$$

Therefore, for each embedding, we now have the following sets of data $\{(\mathcal{F}_a^{\rm GA}, \sigma_a^{\rm G})\}_{a=1}^{N_{\rm E}}$. We refer to this as the gauge-averaged data, of which we have $N_{\rm E}$ data points. We then drew 1000 bootstrap [28] data samples from the gauge-averaged data (giving us a total of $1000 \times N_{\rm E}$ data points), which we denote by $\mathcal{F}_{a,b}^{\rm GA}$ where $a = 1, \ldots, N_{\rm E}$, $b = 1, \ldots, 1000$. In order to account for the fluctuations in the gauge data, for a fixed bootstrap sample b, we add noise (normally distributed with the standard deviation $\sigma_a^{\rm G}$) to every $\mathcal{F}_{a,b}^{\rm GA}$ in the bootstrap sample. For each of the 1000 bootstrap data samples, we calculated the mean:

$$\bar{\mathcal{F}}_b^{\rm GA} = \frac{1}{N_{\rm E}} \sum_{a=1}^{N_{\rm E}} \mathcal{F}_{a,b}^{\rm GA} \,, \quad b = 1, \ldots, 1000 \,. \tag{E5}$$

Therefore we now have a distribution of 1000 means. The mean of the 1000 means corresponds to the data points in our plots, and the standard deviation of the 1000 means is the error bar used in the plots in the main text.

3. Autocorrelation Tests

Correlations between the outputs of different runs on the device could be a possible source of error in our results (such correlations were reported in [7]). To test for this, we use a binning test, which is a simple method to test for autocorrelations in statistical data [47]. Consider a list of n uncorrelated binary numbers $\{x_i\}$ with $P(x_i = 1) = p$. The standard error of the mean for this dataset is $\Delta x \equiv \sqrt{{\rm Var}[x]/n} = \sqrt{p(1-p)/n}$. We bin together the average of consecutive pairs in this list to produce a new list y_i of $n/2$ numbers such that $y_i \in \{0, 0.5, 1\}$. Since $P(y_i = 1) = p^2$, $P(y_i = 0.5) = 2p(1-p)$ and $P(y_i = 0) = (1-p)^2$, the error in the mean of this derived list is $\Delta y = \sqrt{p(1-p)/n} = \Delta x$. If however, the list were correlated such that $P(x_{i+1} = 1 \mid x_i = 1) = q \neq p$, then $\Delta y = \sqrt{(p + q - p^2 - q^2)/(2n)} \neq \Delta x$. The idea of the binning test easily follows: keep on binning data with larger bin sizes until the error in the means converges to a constant value. The minimal bin size where this occurs is the autocorrelation length, ξ.

We used the binning test on all 256 different states for the $N = 8$ problem. For each state, we generated a list of 1000 binary numbers $\{x_i\}$ such that $x_i = 1$ when that state was read from the D-Wave device and $x_i = 0$ otherwise. The proba-

bility of occurrence of the state is denoted by $\bar{x}$ and Δx is its error. We found that the error in the mean does not change appreciably with the size of bins used. This indicates that the autocorrelation length for any state in our system is zero, and there are no significant autocorrelations in our data. Figure 22 shows a few representative cases from the data collected using the "in-cell embeddings" strategy for various choices of α and random gauge choices.

The *Wald-Wolfowitz runs test* is a standard statistical test for autocorrelations. We tested the null hypothesis, H_0, that the sequence in consideration was generated in an unbiased manner. The Wald-Wolfowitz test relies on comparing the number of "runs" in the dataset to a normal distribution of runs. A run is defined as consecutive appearance of same state. In our dataset of binary valued sequences, a run occurs every time there is a series of either 0's or 1's. For example, the sequence 01110010011100011010 0 contains 6 runs of 0 and 5 runs of 1. The total number of runs is 11. Let R be the number of runs in the sequence, N_1 be the number of times value 1 occurs and N_0 be the number of times value 0 occurs. (In our example, $R = 11$, $N_1 = 10$ and $N_0 = 11$.) It can be shown that if the sequence were unbiased, the average and the standard deviation of the number of runs would be given by [48]

$$\bar{R} = \frac{2N_1N_0}{N_1 + N_0} + 1, \tag{E6}$$

$$\sigma_R^2 = \frac{2N_0N_1(2N_1N_0 - N_1 - N_0)}{(N_1 + N_0)^2(N_1 + N_0 - 1)} \tag{E7}$$

The test statistic is $Z = \frac{R-\bar{R}}{\sigma_R}$. At 5% significance level, the test would reject the null hypothesis if $|Z| > 1.96$ (in this case the obtained value of the number of runs differs significantly from the number of runs predicted by null hypothesis).

We applied the Wald-Wolfowitz test to the binary sequences used in the binning test. We found that for each value of α, fewer than 0.01% of the sequences failed the Wald-Wolfowitz test. For example, 112 sequences for $\alpha = 1$, 343 sequences for $\alpha = 0.35$ and 195 sequences for $\alpha = 0.1$ failed the test. The total number of such sequences tested for each value of α were $256 \times 56 \times 256 \approx 3.6 \times 10^6$. This suggests once more that autocorrelations do not affect our dataset significantly.

4. Correcting control errors

Under a closed system evolution all the cluster states end up with an identical population. The same is true if we compute the populations using the ME for an independent bath model. Only when we make $|J|$ and $|h|$ unequal do we observe that the symmetry between the cluster states is broken. This is shown in Fig. 23 using ME calculations, where the population of the cluster-state splits by Hamming distance. We give a perturbation theory argument explaining this phenomenon in the next subsection (Appendix E 5).

Interestingly, the experimental data for the final populations of the cluster-states displays a pronounced "step" structure, clearly visible in Fig. 25(a). The observed steps correspond to an organization of the cluster-states in terms of their Hamming distance from the isolated state, and agrees with the ordering observed in Fig. 23. Thus, the step structure can be explained if, in spite of the fact that for all gauges we set $|h_i|/|J_{ij}| = 1$, in reality there is a systematic error causing $|h_i| < |J_{ij}|$. Such an error would arise if the ratio of $B(t)|h_i|$ and $B(t)|J_{ij}|$ is not kept fixed throughout the annealing, where $B(t)$ is the annealing schedule (shown in Fig. 1). Moreover, such an error would not be unexpected, as the local fields (an inductance) and couplers (a mutual inductance) are controlled by physically distinct devices [2]. Figure 23 and Appendix E 5 provide theoretical support for this hypothesis.

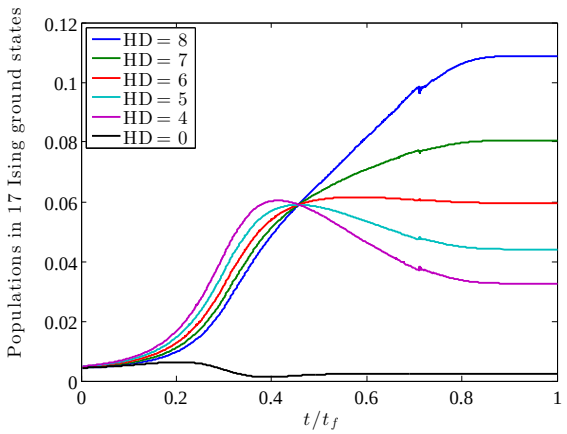

FIG. 23. Master equation results for the populations of the 17 Ising ground states, with $|h| = 0.981|J|$, $t_f = 20\,\mu s$, and $\kappa = 1.27 \times 10^{-4}$. The cluster-states split by Hamming distance from the isolated state (bottom curve), in agreement with the experimental results shown in Fig. 24(a).

$\lvert h_i\rvert$	$\lvert J_{ij}\rvert$	% Change	Absolute Change
1	0.9810	-1.90	-0.0190
6/7	0.8440	-1.53	-0.0131
5/7	0.7040	-1.44	-0.0103
4/7	0.5655	-1.04	-0.0059
3/7	0.4265	-0.48	-0.0021
2/7	0.2850	-0.25	-0.0007
1/7	0.1420	-0.60	-0.0009

TABLE I. Optimized $|J_{ij}|$ values for a given $|h_i|$ value, yielding the flat population structure shown in Fig. 24(b). The systematic corrections are of the order of 1%, smaller than the random control errors of 5%.

The next question is whether we can mitigate this type of error. To do so we introduce a simple optimization technique. Specifically, we can compensate for $|h_i| < |J_{ij}|$ and fine-tune the values of h and J to nearly eliminate the step structure for various values of the energy scale factor α. We show this in Fig. 24(b). The corresponding optimized values are given in Table I, where the compensation reverses the inequality to $|h_i| > |J_{ij}|$.

We have further checked that the same fine-tuning tech-

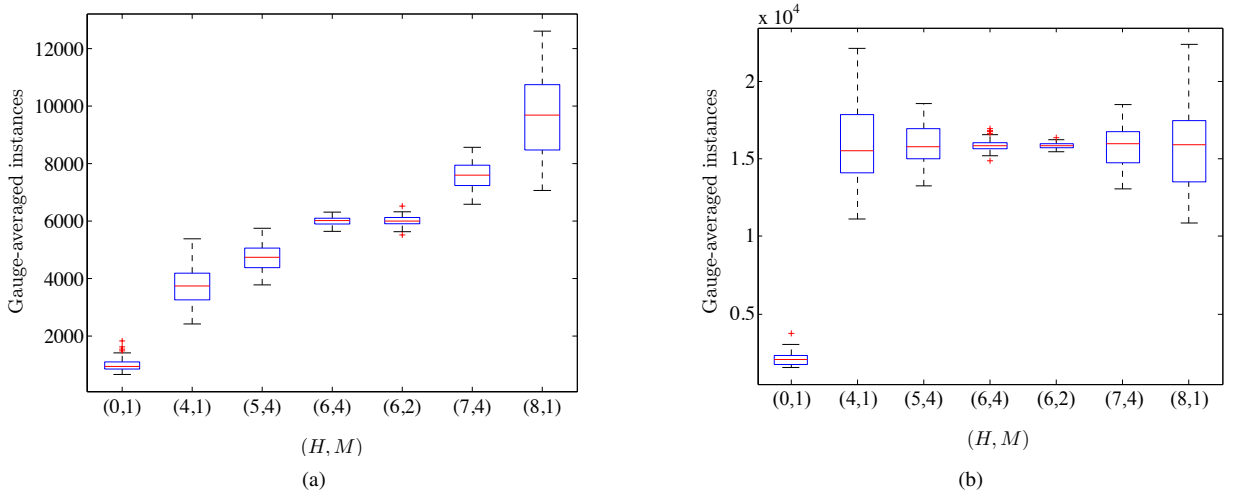

FIG. 24. Statistical box plot of the gauge-averaged occurrences before (left) and after (right) optimization of J_{ij}, for $\alpha = 1$, $t_f = 20\,\mu s$. The horizontal axis label indicates the Hamming distance (H) from the isolated state and the multiplicity (M) of the cluster-states at each value of H. States that are equivalent up to 90° rotations are grouped together. For example, there are 4 rotationally equivalent cluster-states that have two adjacent outer qubits pointing down, while the other two are pointing up. Only the $H = 6$ case splits into two rotationally inequivalent sets. Note the clear step structure in the cluster-states ($H > 0$) in (a), while in (b) the population of the cluster-states is nearly perfectly equal. (a) Data taken with the random parallel embeddings strategy. (b) Data taken using the in-cell embeddings strategy, with the optimized values of the couplings given in Table I. The same optimization removes the step structure from data taken with the random parallel embeddings strategy (not shown).

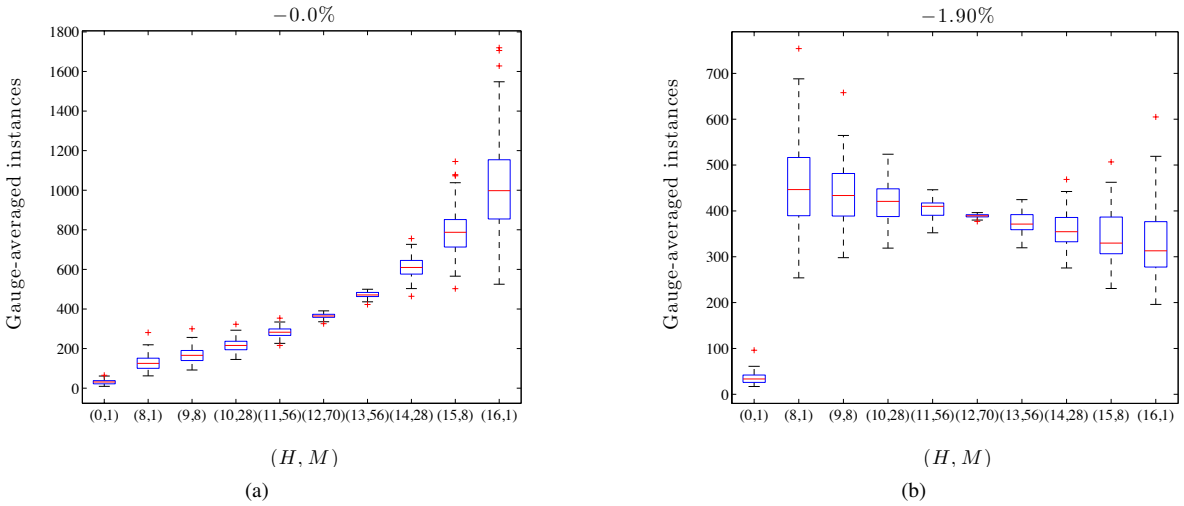

FIG. 25. Ground states population for the 16-spin Hamiltonian before and after optimization. (a) Box plot of the populations before optimization. (b) Box plot of the populations after a -1.9% adjustment to the value of $|J|$, while $|h| = 1$. Data taken with the random parallel embeddings strategy.

nique suppresses the step structure seen in the 16-spin problems, as can be seen in Fig. 25. Note how the step structure in the case of a larger number of spins (left panel) is even more pronounced than in the 8-spin case, shown in Fig. 24(a). By adjusting the value of J while keeping $|h| = 1$ we can reduce the step structure, as shown in the center and right panels of Fig. 25.

With the exception of Fig. 24(a) and Fig. 25, all the experimental data presented here was collected using these optimal values. We note that this gives rise to the interesting possibility of using this "step-flattening" technique to more precisely calibrate the device. We emphasize that this control error has little effect on the suppression/enhancement of the isolated state, as can be seen in Fig. 26.

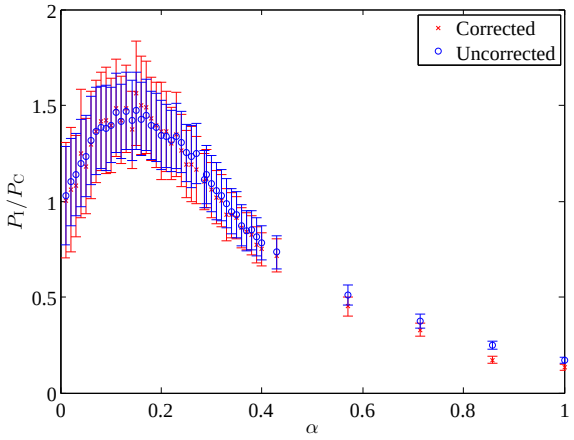

FIG. 26. Ratio of isolated state population to average population in the cluster-states as a function of the energy scale factor α, at a fixed annealing time of $t_f = 20\mu s$. Shown are the ratios calculated with both uncorrected and corrected values of J (as per Table I), the latter tuned to flatten the steps seen in the population of the cluster states. Error bars represent the standard error of the mean value of the ratio estimated using bootstrapping.

5. The $|J| \neq |h|$ case and the splitting of the cluster-states by Hamming distance

We show that the ground state degeneracy is broken by Hamming distance from the isolated state when the local fields are perturbed to smaller absolute values.

Consider a situation where all the local fields are perturbed so that for the outer spins $h_i = -1 + \delta h$ $(1 \leq i \leq 4)$ and for the core spins $h_i = 1 - \delta h$ $(5 \leq i \leq 8)$. Therefore $|h_i| < |J_{ij}| = 1$ and the perturbation to the quantum signature Hamiltonian $H_{\rm I} = -\sum_{i\in\mathcal{V}} h_i\sigma_i^z - \sum_{(i,j)\in\mathcal{E}} J_{ij}\sigma_i^z\sigma_j^z$ [Eq. (2)] can be written as:

$$V = -\delta h\left(\sum_{i=1}^{4}\sigma_i^z - \sum_{i=5}^{8}\sigma_i^z\right) \tag{E8}$$

All the cluster states have their core spins in the $|0\rangle$ state, so V increases all their energies by $4\delta h$. The perturbation acting on the core spins, however, breaks the degeneracy by Hamming distance. The contribution from this term is given by $-(n_0 - n_1)\delta h$ where $n_{0/1}$ is the number of outer spins in the $|0\rangle$ / $|1\rangle$ state. Therefore the energy of the $|0000\,0000\rangle$ state is unchanged (it becomes the unique ground state), while the energy of the $|1111\,0000\rangle$ state increases by $8\delta h$, so it becomes the least populated among the cluster states. Consequently the final population of the cluster states becomes ordered by Hamming distance from the isolated state $|1111\,1111\rangle$.

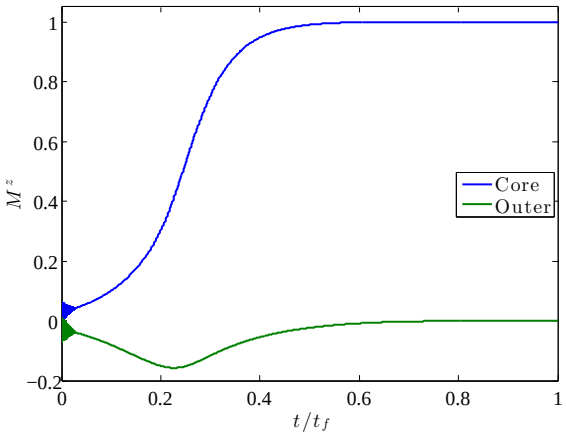

(a) Closed system

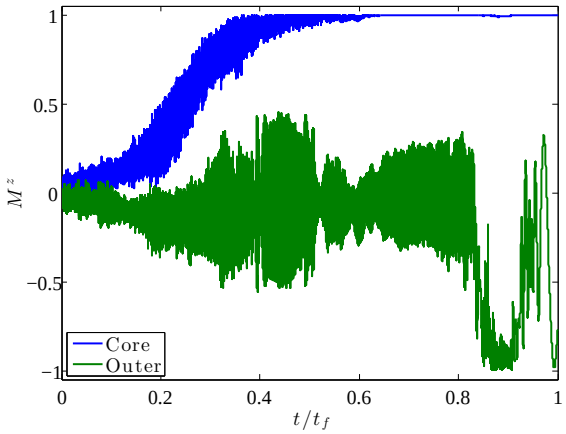

(b) Open system

FIG. 27. Evolution of a core (blue) and outer (green) spin with $t_f = 20\,\mu s$, subject to the O(3) spin-dynamics model with $\alpha = 1$. All spins start with $M^x = 1$, $M^y = M^z = 0$, i.e., point in the x direction. (a) Closed system case given by Eq. (F17). (b) Open system case given by Eq. (F19). Rapid oscillations at the beginning of the evolution in (a) are because the initial conditions used are not exactly the ground state of the system [because of the finite $B(0)$]. In (b), Langevin parameters are $k_BT/\hbar = 2.226\,\text{GHz}$ and $\chi = 10^{-6}$.

Appendix F: Derivation of the O(3) spin-dynamics model

1. Closed system case

Here we present the standard path integral derivation of the O(3) model. Let us introduce the tensor product state of coherent spin-1/2 states

$$|\Omega(t)\rangle = \otimes_i \left(\cos(\theta_i(t)/2)\,|0\rangle_i + \sin(\theta_i(t)/2)e^{i\phi_i(t)}\,|1\rangle_i\right). \tag{F1}$$

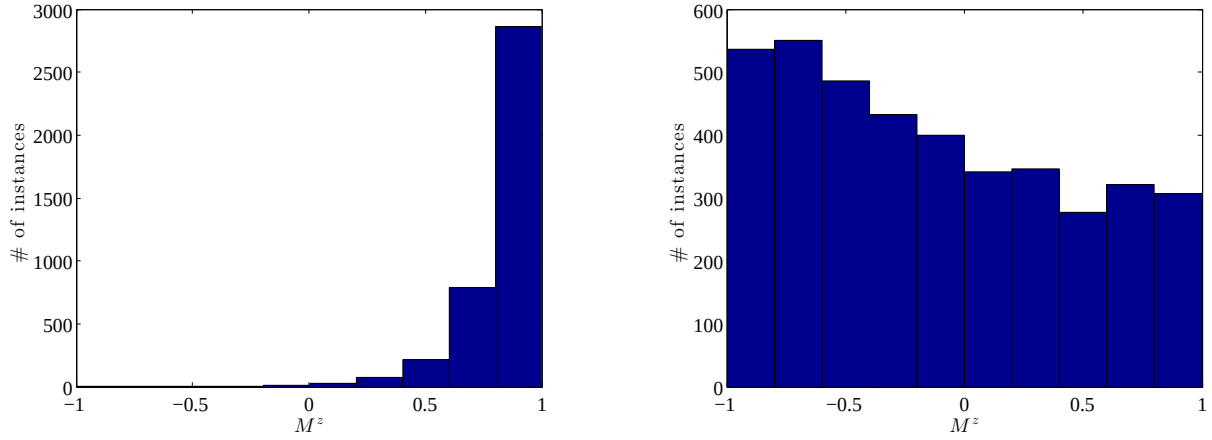

(a) Core spins

(b) Outer spins

FIG. 28. Distribution of M^z at the end of the evolution for all (a) core and (b) all outer spins for $\alpha = 1$. Langevin parameters are $k_B T/\hbar = 2.226\,\text{GHz}$ and $\chi = 10^{-3}$. Data collected using 1000 runs of Eq. (F19).

We consider the amplitude associated with beginning in $|\Omega(0)\rangle = \otimes_i |\Omega_i(0)\rangle$ and ending in $|\Omega(t_f)\rangle$:

$$\mathcal{A} = \langle\Omega(t_f)| T_+ e^{-\frac{i}{\hbar}\int_0^{t_f} H(t)dt} |\Omega(0)\rangle\,, \tag{F2}$$

where T_+ represents time-ordering. We write the integral in terms of a Riemann sum:

$$\int_0^{t_f} H(t)dt = \lim_{\nu\to\infty} \sum_{n=0}^{\nu-1} H(t_n)\Delta t, \tag{F3}$$

where $\Delta t = t_f/\nu$ and $t_n = n\Delta t$, and then perform a Trotter slicing:

$$T_+ e^{-\frac{i}{\hbar}\int_0^{t_f} H(t)dt} = \prod_{n=0}^{\nu-1} e^{-\frac{i}{\hbar}H(t_n)\Delta t} + O(\Delta t^2) \tag{F4}$$

We now introduce an overcomplete set of spin-coherent states (F1) between the Trotter slices

$$\mathbb{1} = \int d\Omega |\Omega\rangle\langle\Omega|, \tag{F5}$$

where for general spin S

$$d\Omega = \prod_i \frac{2S+1}{4\pi} \sin\theta_i d\phi_i d\theta_i, \tag{F6}$$

so that we have:

$$\mathcal{A} = \int d\Omega_1 \cdots \int d\Omega_{\nu-1} \prod_{n=1}^{\nu} \langle\Omega_n| e^{-\frac{i}{\hbar}H_{n-1}\Delta t} |\Omega_{n-1}\rangle + O(\Delta t^2)\,, \tag{F7}$$

where we have denoted $\Omega_\nu \equiv \Omega(t_f)$, $\Omega_0 \equiv \Omega(0)$, and $H_n \equiv H(t_n)$. To the same order of approximation we can write:

$$\langle\Omega_n| e^{-\frac{i}{\hbar}H_{n-1}\Delta t} |\Omega_{n-1}\rangle = \tag{F8a}$$

$$\langle\Omega_n| \left(\mathbb{1} - \frac{i}{\hbar}H_{n-1}\Delta t\right) |\Omega_{n-1}\rangle + O(\Delta t^2) = \tag{F8b}$$

$$\langle\Omega_n|\Omega_{n-1}\rangle \left(1 - \frac{i\Delta t}{\hbar}\frac{\langle\Omega_n| H_{n-1} |\Omega_{n-1}\rangle}{\langle\Omega_n|\Omega_{n-1}\rangle}\right) + O(\Delta t^2). \tag{F8c}$$

Let us assume differentiability of the states Ω_n and the Hamiltonian H_n so that we can write:

$$|\Omega_{n-1}\rangle = |\Omega_n\rangle - \Delta t\partial_t |\Omega_n\rangle + O(\Delta t^2) \tag{F9a}$$

$$H_{n-1} = H_n - \Delta t\partial_t H_n + O(\Delta t^2). \tag{F9b}$$

Using this differentiability on the overlap, we have:

$$\langle\Omega_n|\Omega_{n-1}\rangle = \langle\Omega_n| (|\Omega_n\rangle - \Delta t\partial_t |\Omega_n\rangle) + O(\Delta t^2) \tag{F10a}$$

$$= 1 - \Delta t \langle\Omega_n| \partial_t |\Omega_n\rangle + O(\Delta t^2) \tag{F10b}$$

$$= \exp\left(-\Delta t \langle\Omega_n| \partial_t |\Omega_n\rangle\right) \tag{F10c}$$

Likewise, using this differentiability on the matrix element of the Hamiltonian, we have:

$$\Delta t \langle\Omega_n| H_{n-1} |\Omega_{n-1}\rangle = \tag{F11a}$$

$$\Delta t \langle\Omega_n| (H_n - \Delta t\partial_t H_n)(|\Omega_n\rangle - \Delta t\partial_t |\Omega_n\rangle) + O(\Delta t^2) = \tag{F11b}$$

$$\Delta t \langle\Omega_n| H_n |\Omega_n\rangle + O(\Delta t^2) = \tag{F11c}$$

$$\exp(\Delta t \langle\Omega_n| H_n |\Omega_n\rangle). \tag{F11d}$$

Putting these results together, we have for the amplitude:

$$\mathcal{A} = \int d\Omega_1 \cdots \int d\Omega_{\nu-1} \times \tag{F12a}$$

$$e^{\frac{i}{\hbar}\Delta t \sum_{n=1}^{\nu}(i\hbar\langle\Omega_n|\partial_t|\Omega_n\rangle - \langle\Omega_n|H_n|\Omega_n\rangle)} + O(\Delta t^2) \tag{F12b}$$

$$= \int \mathcal{D}\Omega \exp\left[\frac{i}{\hbar}\int dt \left(i\hbar \langle\Omega| \partial_t |\Omega\rangle - \langle\Omega| H(t) |\Omega\rangle\right)\right] \tag{F12c}$$

$$= \int \mathcal{D}\Omega \, e^{\frac{i}{\hbar}S[\Omega]} \tag{F12d}$$

where we have taken the continuum limit such that $\Omega_n \to \Omega(t)$ and introduced the action

$$S[\Omega] = \int dt \left(i\hbar \langle\Omega| \partial_t |\Omega\rangle - \langle\Omega| H(t) |\Omega\rangle\right) . \tag{F13}$$

For simplicity, let us now work in units of $\hbar = 1$. Using Eq. (F1) we can write the first term in the action as:

$$i \langle\Omega| \partial_t |\Omega\rangle = -\frac{1}{2}\sum_i (1 - \cos\theta_i) \frac{d\phi_i}{dt} \tag{F14}$$

The Euler-Lagrange equations of motion

$$\frac{d}{dt}\left(\frac{\partial S}{\partial \dot{\phi}_i}\right) - \frac{\partial S}{\partial \phi_i} = 0 , \tag{F15a}$$

$$\frac{d}{dt}\left(\frac{\partial S}{\partial \dot{\theta}_i}\right) - \frac{\partial S}{\partial \theta_i} = 0 \tag{F15b}$$

extremize the action and yield the semi-classical saddle point approximation:

$$\frac{1}{2}\sin\theta_i \frac{d}{dt}\theta_i - \frac{\partial}{\partial \phi_i}\langle\Omega| H(t) |\Omega\rangle = 0 , \tag{F16a}$$

$$-\frac{1}{2}\sin\theta_i \frac{d}{dt}\phi_i - \frac{\partial}{\partial \theta_i}\langle\Omega| H(t) |\Omega\rangle = 0 . \tag{F16b}$$

These are the equations of motion for the $O(3)$ model.

For a Hamiltonian of the form of Eq. (2), the equations of motion become, in terms of the magnetization $\vec{M} = \mathrm{Tr}\,(\vec{\sigma}\rho)$,

$$\frac{d}{dt}\dot{\vec{M}}_i = -\vec{H}_i \times \vec{M}_i \tag{F17a}$$

$$\vec{H}_i \equiv 2A(t)\hat{x} + 2\alpha B(t)\left(h_i + \sum_{j\neq i} J_{ij}\vec{M}_j \cdot \hat{z}\right)\hat{z} , \tag{F17b}$$

where we have already included the α dependence. Using the DW2 annealing schedule in Fig. 1, we plot the evolution of the spin system in Fig. 27(a). This figure shows that the system evolves to what we would we call a cluster state. Namely, the core spins have $M^z = 1$, i.e., are in the $|0\rangle$ state, and the outer spins have $M^z = 0$. Since the outer spins have eigenvalues ± 1 under σ^z with equal probability, having the average equal zero is consistent with having an equal distribution among the cluster states. This suppression of the isolated state result is consistent with the QA evolution, and was used in Ref. [9] to critique the conclusion of Ref. [6] that the experimental evidence is consistent with quantum evolution. In the next subsection we discuss the effect of adding thermal noise and a dependence on the energy scale factor α. Both of these lead to to the conclusion that the O(3) model is inconsistent with the experimental results after all.

2. Open system case: Langevin Equation

Now that we have our "classical" model, we introduce a thermal bath by extending the equations of motion to an appropriately generalized (Markovian) spin-Langevin equation [29, 30],

$$\frac{d}{dt}\vec{M}_i = -\left(\vec{H}_i + \vec{\xi}(t) - \chi\frac{d}{dt}\vec{M}_i\right) \times \vec{M}_i , \tag{F18}$$

with the Gaussian noise $\vec{\xi}$ satisfying $\langle\xi_i(t)\rangle = 0$ and $\langle\xi_i(t)\xi_i(t')\rangle = 2k_B T\chi\delta(t-t')$. One can simplify Eq. (F18) by perturbatively inserting $\frac{d}{dt}\vec{M}_i = -\vec{H}_i \times \vec{M}_i$ into the "friction" term to get:

$$\frac{d}{dt}\vec{M}_i = -\left(\vec{H}_i + \vec{\xi}(t) + \chi\vec{H}_i \times \vec{M}_i\right) \times \vec{M}_i , \tag{F19}$$

which gives rise to a "Landau-Lifshitz" friction term [30, 31] and is the evolution equation (7) given in the main text.

An example of the resulting evolution for $\alpha = 1$ is shown in Fig. 27(b). Note that the M^z value of the outer spins does not converge to 0, unlike the closed system case shown in Fig. 27(a). This is not accidental: while the core spins prefer the $|0\rangle$ state [$M^z = 1$, Fig. 28(a)], the outer spins prefer the $|1\rangle$ state, i.e., the median occurs at $M^z < 0$, as is clearly visible in Fig. 28(b).

To understand this, consider first the closed system (no thermal noise) case and note that for $t > 0.6t_f$, the transverse field is almost completely turned off. Therefore, if one treats $\langle\Omega| H |\Omega\rangle$ [Eq. (F16)] as a potential, the cluster states' outer spins are free to rotate (i.e., with no energy cost) when the core spins are pinned at $M^z_C = 1$, leading to $M^z_O = 0$ (the C and O subscripts stand for "core" and "outer", respectively). However, in the open system case (in the presence of thermal noise) the core spins are not fixed at $M^z_C = 1$, and $M^z_O = -1$ becomes energetically favorable for the outer spins. To see why, consider the case of a single pair of core and outer spins. In this case, the Ising potential is simply $-(h_O M^z_O + h_C M^z_C + J_{OC} M^z_O M^z_C) = M^z_O - M^z_C - M^z_O M^z_C$. When $M^z_C = 1$, the dependence on M^z_O vanishes so the outer spin is free to rotate, however when $M^z_C \neq 1$ (as happens when thermal noise is present), this Ising potential is minimized when $M^z_O = -1$. This reasoning matches the simulation results, shown in Fig. 28(b), where the distribution of the outer spins is peaked close to $M^z_O = -1$. This feature is absent in the experimental results [see, e.g., Fig. 24(b)] and by itself already invalidates the SD model.

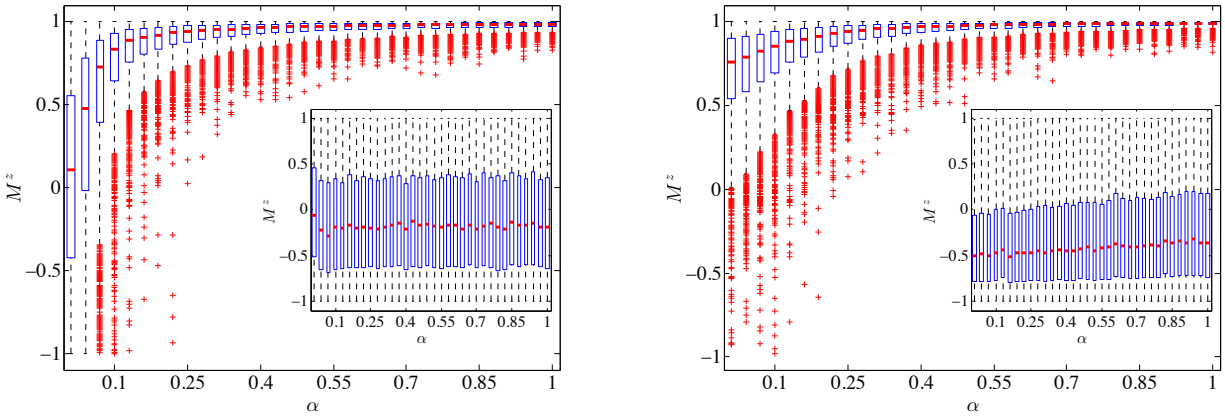

(a) $\chi = 10^{-1}$ (b) $\chi = 10^{-5}$

FIG. 29. Statistical box plot of the z component for all core qubits (main plot) and all outer qubits (inset) at $t = t_f = 20\mu s$. The red bar is the median, the blue box corresponds to the lower and upper quartiles, respectively, the segment contains most of the samples, and the $+$'s are outliers [32]. The data is taken for 1000 runs of Eq. (F19) with Langevin parameters $k_BT/\hbar = 2.226\,\mathrm{GHz}$ (to match the operating temperature of the DW2) and (a) $\chi = 10^{-1}$ and (b) $\chi = 10^{-5}$. The $\chi = 10^{-3}$ is shown in Fig. 11 in the main text. This illustrates that the results do not depend strongly on the choice of χ.

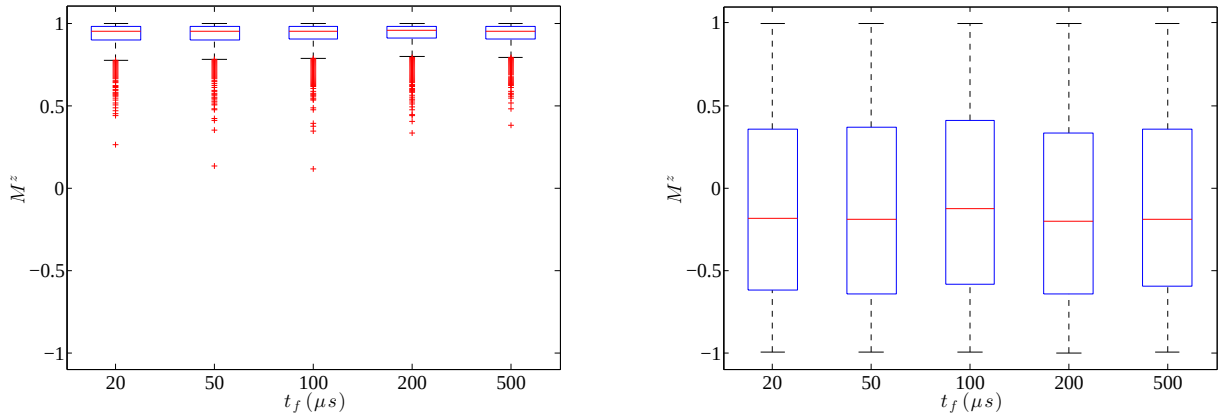

(a) Core spins (b) Outer spins

FIG. 30. Distribution of M^z at the end of the evolution for all core and all outer spins (i.e. the values of all core spins and all outer spins are included in each respective box plot) for $\alpha = 2/7$. Langevin parameters are $k_BT/\hbar = 2.226\,\mathrm{GHz}$ and $\chi = 10^{-3}$. Data collected using 1000 runs of Eq. (F19). Note that the t_f-axis scale is not linear.

The dependence on α is given in Fig. 11 (main text). We observe that as α is decreased, the median value of the core spins and outer spins does not significantly change. However, we do observe a very slow decrease away from $M^z = 1$ for the core spins. A larger effect is the appearance of more outliers as α decreases, which is consistent with the system being able to explore states away from the cluster states. However, we emphasize that the majority of the states observed are cluster states and not the isolated state (in contradiction with the experimental results).

We have checked the dependence of our results on the friction parameter χ. In Fig. 29(a) we see for sufficiently large χ ($> 10^{-3}$), the median values are not affected significantly by changing χ. For sufficiently small χ [Fig. 29(b)] we observe that the median value of the core spins does not deviate very far from 1, and the median of the outer spins appears to shift even further towards $M^z_O = -1$.

We have also checked the dependence on the annealing time. As shown in Fig. 30, there is no significant change in the median for either the core or the outer spins, suggesting that (over the range of annealing times studied) the system does not fully thermalize.

[1] B. W. Reichardt, F. Unger, and U. Vazirani, Nature **496**, 456 (2013).

[2] M. W. Johnson, P. Bunyk, F. Maibaum, E. Tolkacheva, A. J. Berkley, E. M. Chapple, R. Harris, J. Johansson, T. Lanting, I. Perminov, E. Ladizinsky, T. Oh, and G. Rose, Superconductor Science and Technology **23**, 065004 (2010).

[3] A. J. Berkley, M. W. Johnson, P. Bunyk, R. Harris, J. Johansson, T. Lanting, E. Ladizinsky, E. Tolkacheva, M. H. S. Amin, and G. Rose, Superconductor Science and Technology **23**, 105014 (2010).

[4] R. Harris, M. W. Johnson, T. Lanting, A. J. Berkley, J. Johansson, P. Bunyk, E. Tolkacheva, E. Ladizinsky, N. Ladizinsky, T. Oh, F. Cioata, I. Perminov, P. Spear, C. Enderud, C. Rich, S. Uchaikin, M. C. Thom, E. M. Chapple, J. Wang, B. Wilson, M. H. S. Amin, N. Dickson, K. Karimi, B. Macready, C. J. S. Truncik, and G. Rose, Phys. Rev. B **82**, 024511 (2010).

[5] N. G. Dickson, M. W. Johnson, M. H. Amin, R. Harris, F. Altomare, A. J. Berkley, P. Bunyk, J. Cai, E. M. Chapple, P. Chavez, F. Cioata, T. Cirip, P. deBuen, M. Drew-Brook, C. Enderud, S. Gildert, F. Hamze, J. P. Hilton, E. Hoskinson, K. Karimi, E. Ladizinsky, N. Ladizinsky, T. Lanting, T. Mahon, R. Neufeld, T. Oh, I. Perminov, C. Petroff, A. Przybysz, C. Rich, P. Spear, A. Tcaciuc, M. C. Thom, E. Tolkacheva, S. Uchaikin, J. Wang, A. B. Wilson, Z. Merali, and G. Rose, Nat. Commun. **4**, 1903 (2013).

[6] S. Boixo, T. Albash, F. M. Spedalieri, N. Chancellor, and D. A. Lidar, Nat Commun **4** (2013).

[7] S. Boixo, T. F. Rønnow, S. V. Isakov, Z. Wang, D. Wecker, D. A. Lidar, J. M. Martinis, and M. Troyer, Nat Phys **10**, 218 (2014).

[8] S. Aaronson, "D-Wave: Truth finally starts to emerge," .

[9] J. A. Smolin and G. Smith, arXiv:1305.4904 (2013).

[10] L. Wang, T. F. Rønnow, S. Boixo, S. V. Isakov, Z. Wang, D. Wecker, D. A. Lidar, J. M. Martinis, and M. Troyer, (2013), arXiv:1305.5837.

[11] T. Albash, S. Boixo, D. A. Lidar, and P. Zanardi, New J. of Phys. **14**, 123016 (2012).

[12] S. W. Shin, G. Smith, J. A. Smolin, and U. Vazirani, ArXiv e-prints (2014), arXiv:1401.7087 [quant-ph].

[13] T. Lanting, A. J. Przybysz, A. Y. Smirnov, F. M. Spedalieri, M. H. Amin, A. J. Berkley, R. Harris, F. Altomare, S. Boixo, P. Bunyk, N. Dickson, C. Enderud, J. P. Hilton, E. Hoskinson, M. W. Johnson, E. Ladizinsky, N. Ladizinsky, R. Neufeld, T. Oh, I. Perminov, C. Rich, M. C. Thom, E. Tolkacheva, S. Uchaikin, A. B. Wilson, and G. Rose, arXiv:1401.3500 (2014).

[14] J. S. Bell, *Speakable and Unspeakable in Quantum Mechanics* (Cambridge University Press, Cambridge, UK, 1987).

[15] S. Kirkpatrick, C. D. Gelatt, and M. P. Vecchi, Science **220**, 671 (1983).

[16] A. B. Finnila, M. A. Gomez, C. Sebenik, C. Stenson, and J. D. Doll, Chemical Physics Letters **219**, 343 (1994).

[17] T. Kadowaki and H. Nishimori, Phys. Rev. E **58**, 5355 (1998).

[18] J. Brooke, D. Bitko, T. F. Rosenbaum, and G. Aeppli, Science **284**, 779 (1999).

[19] J. Brooke, T. F. Rosenbaum, and G. Aeppli, Nature **413**, 610 (2001).

[20] W. M. Kaminsky and S. Lloyd, in *Quantum Computing and Quantum Bits in Mesoscopic Systems*, edited by A. Leggett, B. Ruggiero, and P. Silvestrini (Kluwer Academic/Plenum Publ., 2004) arXiv:quant-ph/0211152.

[21] M. W. Johnson, M. H. S. Amin, S. Gildert, T. Lanting, F. Hamze, N. Dickson, R. Harris, A. J. Berkley, J. Johansson, P. Bunyk, E. M. Chapple, C. Enderud, J. P. Hilton, K. Karimi, E. Ladizinsky, N. Ladizinsky, T. Oh, I. Perminov, C. Rich, M. C. Thom, E. Tolkacheva, C. J. S. Truncik, S. Uchaikin, J. Wang, B. Wilson, and G. Rose, Nature **473**, 194 (2011).

[22] S. Morita and H. Nishimori, J. Math. Phys. **49**, 125210 (2008).

[23] A. Das and B. K. Chakrabarti, Rev. Mod. Phys. **80**, 1061 (2008).

[24] Y.-H. Lee and B. J. Berne, The Journal of Physical Chemistry A **104**, 86 (1999).

[25] A. M. Childs, E. Farhi, and J. Preskill, Phys. Rev. A **65**, 012322 (2001).

[26] M. S. Sarandy and D. A. Lidar, Physical Review Letters **95**, 250503 (2005).

[27] M. H. S. Amin, P. J. Love, and C. J. S. Truncik, Phys. Rev. Lett. **100**, 060503 (2008).

[28] B. Efron and R. Tibshirani, *An Introduction to the Bootstrap* (Taylor & Francis, 1994).

[29] A. Jayannavar, Zeitschrift für Physik B Condensed Matter **82**, 153 (1991).

[30] R. Kubo and N. Hashitsume, Progress of Theoretical Physics Supplement **46**, 210 (1970).

[31] L. D. Landau and E. M. Lifshitz, Phys. Z. Sowjetunion **8**, 153 (1935).

[32] M. Frigge, D. C. Hoaglin, and B. Iglewicz, The American Statistician **43**, 50 (1989).

[33] T. Rønnow and M. Troyer, private communications.

[34] M. Nielsen and I. Chuang, *Quantum Computation and Quantum Information*, Cambridge Series on Information and the Natural Sciences (Cambridge University Press, 2000).

[35] G. Vidal and R. F. Werner, Physical Review A **65**, 032314 (2002).

[36] L. A. Wu, M. S. Sarandy, and D. A. Lidar, Physical Review Letters **93**, 250404 (2004).

[37] H. G. Katzgraber, F. Hamze, and R. S. Andrist, arXiv:1401.1546 (2014).

[38] I. de Vega, M. C. Bañuls, and A. Pérez, New J. of Phys. **12** (2010).

[39] M. H. S. Amin, D. V. Averin, and J. A. Nesteroff, Phys. Rev. A **79**, 022107 (2009).

[40] K. L. Pudenz, T. Albash, and D. A. Lidar, Nat Commun **5** (2014).

[41] W. Vinci, K. Markström, S. Boixo, A. Roy, F. M. Spedalieri, P. A. Warburton, and S. Severini, arXiv:1307.1114 (2013).

[42] T. F. Rønnow, Z. Wang, J. Job, S. Boixo, S. V. Isakov, D. Wecker, J. M. Martinis, D. A. Lidar, and M. Troyer, arXiv:1401.2910 (2014).

[43] V. Choi, Quant. Inf. Proc. **10**, 343 (2011).

[44] N. Metropolis, A. W. Rosenbluth, M. N. Rosenbluth, A. H. Teller, and E. Teller, J. Chem. Phys. **21**, 1087 (1953).

[45] K. C. Young, R. Blume-Kohout, and D. A. Lidar, Physical Review A **88**, 062314 (2013).

[46] T. Lanting, D-Wave Inc., private communications (2013).

[47] U. Wolff, Computer Physics Communications **156**, 143 (2004).

[48] J. Bradley, *Distribution-free statistical tests* (Prentice-Hall, 1968).